Introductory Notes

The Conference series "Biophysics@Rome", held in Rome in the Tor Vergata research area of CNR, is dedicated to Biophysics and related technologies, and is already in its second edition, having had in May 2014 a considerable success in terms of membership and contributions.

The 2015 Edition (28th & 29Th May) ideally bound to the many initiatives organized in the framework of the International Year of Light and Light-based technologies (IYL 2015, http://www.light2015.org), proclaimed on 20th December 2013 by the General Assembly of the United Nations.

In this context, the Conference opening has been dedicated to "light themes", to evidence the role of advanced optical techniques in biophysics, bio-analytics and biomedicine, still preserving the final aim of *Biophysics@Rome* to build a robust bridge between Companies and places traditionally devoted to frontier research. This is actually the spirit that drives the inter-institute initiative of CNR "Tech4Bio", which promotes and organizes the event.

The working group Tech4Bio consists of CNR researchers with different expertise but a common aim of favoring the formation of a scientific network contacting many different and complementary experiences, knowledge and technology, to explore the possibilities of scientific and technological development in the field of Biophysics, Biosensing and Biotechnology.

The group is presently involved in a number of projects and collaborations on biochemistry, advanced microscopy, innovative sensing and diagnostic platforms, nano and micro scale material characterization for biomedical applications, lab and cell-on-chip devices (www.tech4bio.eu).

Biophysics@Rome 2015 has been a renewed important opportunity to discuss innovative solutions in a field in rapid expansion and intended to have a huge social and economic impact.
Next round in 2017!

Tech4Bio group

VOLUME INDEX

Predicting relevant functionally areas within different domains of PDI.

Lisa Beatrice Caruso[a], Fabio Altieri[b], Alfredo Colosimo[a]

Dept. SAIMLAL, Sapienza - Università di Roma, via Alfonso Borelli 50-00161 Rome, Italy

Dept. Biochemical Sciences, A. Rossi Fanelli, Sapienza - Università di *Roma,*. P.le A. Moro, 5 - 00185 *Rome*, Italy

Abstract

A dynamical simulation of the effect of single point mutations in a Disulfide Isomerase Protein has been carried out by means of the Turbine software, namely submitting a network model of the protein to an energy dissipation algorithm. A Principal Component Analysis study of the multidimensional variables produced by Turbine, before and after introducing point mutations in the primary structure, suggests a critical change in the energy dissipation mechanisms, upon substituting the Ala_{403} residue by a Trp. These results greatly simplify planning appropriate experiments to validate the simulation-based mechanisms.

Keywords: network analysis; PDI proteins; Turbine

1. Introduction

Disulfide Isomerases (PDI) were the first protein modifiers characterized as such (Goldberger et al., 1964). Since their discovery, more than 40 years ago, PDI were indicated as dithiol–disulfide oxidoreductases capable of reducing, oxidizing and isomerizing disulfide bonds; subsequently and independently of the redox activity, PDIs were also shown to act as chaperones both in vitro (Cai et al., 1994) and in vivo (McLaughlin et al., 1998). Moreover, most PDIs family members contain two catalytic (named *a* and *a'*) and two non-catalytic (named *b* and *b'*) thioredoxin-like domains, based on the presence or absence, respectively, of a catalytic motif (Alanen et al., 2003) (Figure1).
Understanding PDIs' function was historically hampered by lack of structural information. Over the last years, however, partial and full-length structures have been solved at an increasing pace and their analysis revealed both common features shared by several the family members, as well as unique features of single members, related to substrate and partner binding sites. While their functions in the Endoplasmic Reticulum (ER) have been thoroughly studied, much less is known about their roles in non-ER locations, where they are involved in important biological processes: in some cases the function is related to the redox properties, but in most cases the action mechanism still needs clarification, although the propensity to associate with other proteins or even with DNA might be crucial for their activities (Turano et al., 2002).

Introducing specific mutations along the primary structure is an efficient method to identify residues crucial for structure/function relationships, since even a single mutation in a "hot spot" can (de)stabilize the whole protein structure. Thus, we performed a computational site directed mutagenesis on different areas of a relatively well-known PDI protein, the ERp57 (Frickel et al., 2004). Then, we studied the mutants properties by a network-based modelistic approach, in the aim to identify relevant structural and functional areas. Finally, in order to assess the significance of the bulk of data gathered by our simulations we used a Principal Component Analysis (Jackson, 1991) and standard inferential multivariate statistics.
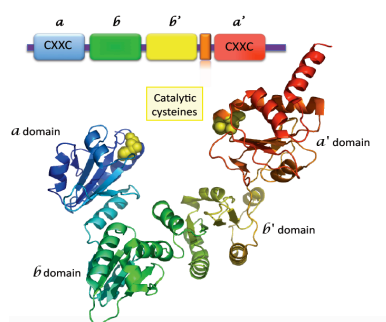
Figure 1 Ribbon diagrams of a PDI with the catalytic domains, a and a', in blue and red, respectively. The cysteines in the active site are shown in space-filling representation. The non-catalytic domains, b and b' are in green and yellow, respectively.

2. Materials and Methods

ERp57: a relevant member of the PDI family
The structure of the crystallized ERp57 in complex with tapasin (PDB id: 3f8u), is the only complete structure currently in the Protein Data Bank for a PDI protein. The site-directed mutagenesis (see Appendix B) was made using the Swiss PDB Viewer. We prepared via this method about 50 mutants for each domain focusing on areas whose importance has been relatively well proven. The topological representation of the proteins, was carried out by the Rinerator software (Doncheva et al., 2011).

A network modelling of protein functions
The power of network based protein modelling lies in the ability to suggest dynamic (functional) mechanisms on the basis of the available static (structural) information. Among the parameters commonly used in network models, we chose the *silencing time* as calculated by the Turbine software tool (Szalay and Csermely, 2013), namely the time needed to dissipate an energy perturbation provided in a specific locus in a process starting from that locus and spreading throughout the molecule. The basic idea behind the Turbine algorithm is that intensive physical variables (e.g. temperature) tend towards an equilibrium according to an exponential decay and that a network with loosely connected modules will dissipate energy slower than a network with tightly interconnected modules. The equation of the model is the following:

$$\frac{dS}{dt} = -\sum_{i=0}^{l}\left(\frac{S-S_i}{2}w_i\right) - D_0$$

where S is the value of the state variable (energy) of the starting node of the edge; *l* is the number of edges (degree) of the current node; S_i is the energy of the node on the other end of the current edge; w_i is the weight of the current edge; D_0 is the dissipation coefficient, which is kept constant for all nodes. The most relevant parameters of the model is the *silencing time* of the i_{th} node, namely the time at which, after the initial perturbation started from node i, all the nodes in the network reach an energy level lower than a pre-set minimal threshold (we selected this threshold as 1, with the dissipation characteristic value (time) also being set to 1).

3. Results

The profiles of silencing times along the primary structures.
The histograms in Figure 2 are related to the silencing times averaged over the primary structure of the whole protein as a consequence of the energy input administered to each single element along the 377 – 485 sequence of the ERp57 *a'* domain (see the legend). Red and blue columns refer to a Trp and a Gly used as substitutions of the native Ala_{403}.
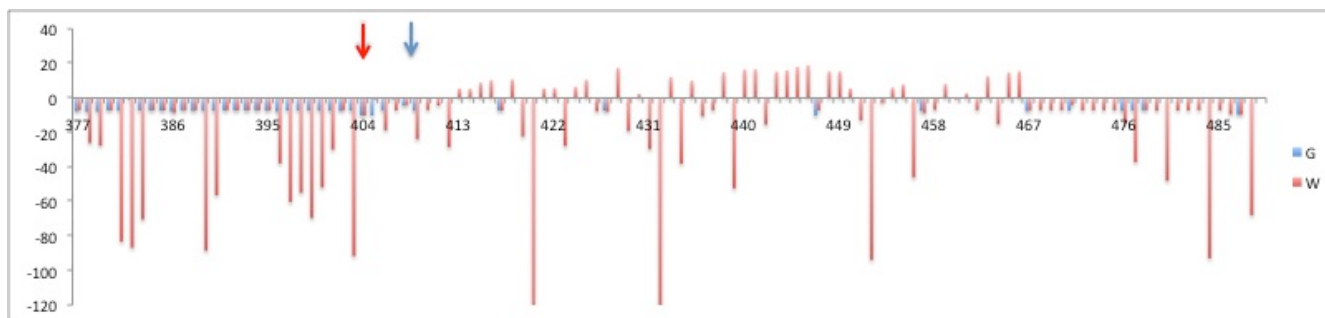
Figure 2. The residue number in the abscissa refer to the AA sequence of the a' domain of ERp57. The columns indicate the difference between WT and mutant species in the averaged silencing times observed over all residues along the primary structure of the whole protein as a consequence of the energy input administered to the single residue in the abscissa. The blue and red columns refer to the mutants obtained using by substituting, respectively, a Glycine or a Tryptophan to the WT residue. Higher spikes correspond to higher differences in silencing time between the WT and the site-specific mutant. The red arrow indicates the location of the mutated residue (Trp_{403} mutant), responsible for the effects shown in the figure.

The blue arrow points to Cys_{409} the main responsible of the catalytic activity of the domain, and the number of high red peaks in the close vicinity of such location indicates the considerable changes induced by the bulky Trp_{403} substituent (red arrow). All in all, the interesting information gathered from the figure concerns: the critical role of the substituent size, as shown by contrasting the quite different effects produce by Gly and Trp .

Quantifying the changes induced by the point mutations.

In order to assess the statistical significance of the asimmetric distribution of peaks observed in figure 2, we designed the following procedure:

1) the 377 – 485 fragment of the protein primary structure corresponding to the a' domain was divided into four subfragments of 27 residues each;

2) each subfragment was considered as a statistical unit described by the values of the silencing times appearing as columns in figure 2;

3) since the columns in figure 2 actually represent differences between WT and mutant proteins, the 4 subfragments can split into 4 couples, and each member of each couple associated to WT or mutant silencing times;

4) the ensuing (8 units x 27 variables) matrix was subjected to an unsupervised clustering algorithm (figure 3, left), and to a PCA (see Appendix B);

5) the first two component obtained by PCA contained about 80% of the total information and figure 3 (middle) shows the projection of the eight statistical units in the PC1-PC2 plane;

6) figure 3 (right) shows the dendrogram obtained as in the left panel, but on the basis of the 27 variables transformed by PCA.
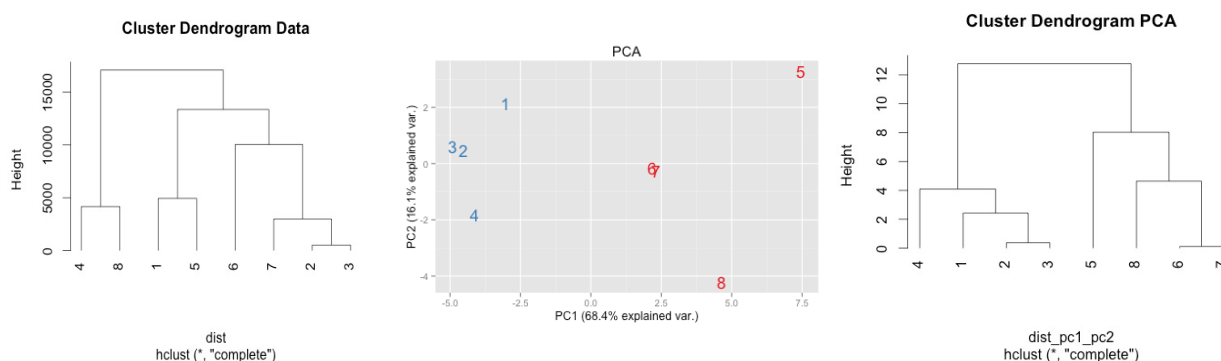

Figure 3 *Clustering of corresponding fragments from WT and mutated PDI in a Principal Component space.*
The 3 panels refer to the ERp57 a' domains (see also Fig 1) and were obtained from a (8 x 27) DATA matrix in which the variables (columns) were the silencing times and the statistical units (rows) were the residues in eight molecular fragments (1 to 4 from the WT and 5 to 8 from a mutant) associated to each domain. A PCA applied to the DATA matrix (middle panel) indicates that in the plane defined by the first and the second principal components (accounting for more than 80% of the information included in the data set) the 1-4 (WT) and the 5-8 (mutant) units are much better separated than by an unsupervised clustering method (left panel). The right panel is a tree-like representation of the PCA induced clustering.

By directly comparing the clusters obtained before (left panel) and after (middle panel) application of the PCA, it can be noticed the substantial improvement in the clustering resolution obtained by latter step: only in the middle panel, in fact, are clearly separated the 1-4 and the 5-8 fragments obtained, respectively, from the WT and the mutant protein.

Discussion

Combining the network approach and the site-directed mutagenesis, revealed a good approach to pick the structure/function mechanistic correlations in one relevant member (ERp57) of the PDI family.

As clearly quantified in figure 3 and Table 1, the first principal component (PCA$_1$) is able to discriminate between WT (1 – 4) and mutant (5 – 8) fragments, while the second principal component (PCA$_2$) further discriminates between the single fragments within each of the two above clusters. Upon considering that the only event responsible for the reported observations is a point mutation induced in a specific location of the AA sequence, the main conclusion in exploring the dynamics of energy distribution within the protein at hand is the extremely high resolution power gained by the combined use of: i) site directed mutagenesis, ii) simulation of the energy dissipation dynamics by the silencing time algorithm and, iii) principal component analysis,

In spite of their ubiquitous presence and vaste range of putative functions, the detailed regulative mechanisms of all PDI family members remain obscure. However we could at least demostrate the high sensitivity of *ERp57* to a single point mutation in a location close to the active site, namely the Ala$_{403}$ → Trp$_{403}$ substitution.

In any case, possible extension of the above conclusion to other members of the PDI family will be only possible by direct experiments of site-directed mutagenesis (in due course). Even more so since the 3D data used in our network modeling actually refer to the *ERp57*-tapasine complex, in which the molecular flexibility, and hence the subtle regulation mechanisms, of the 'naked' *ERp57* molecule, could have been masked.
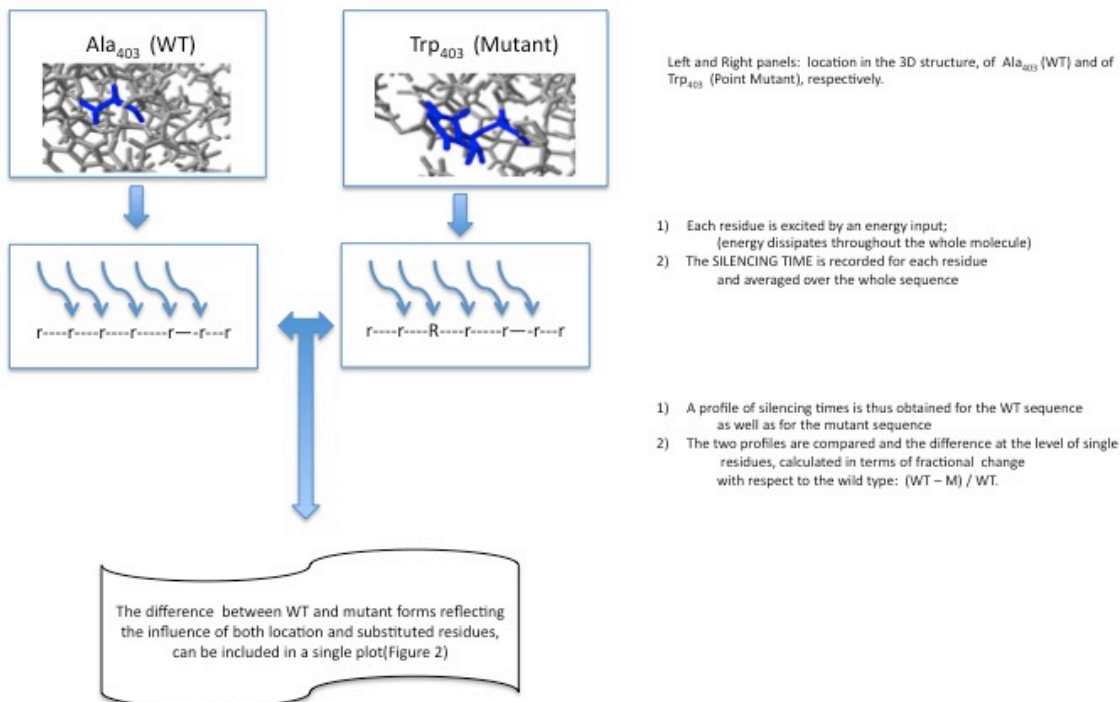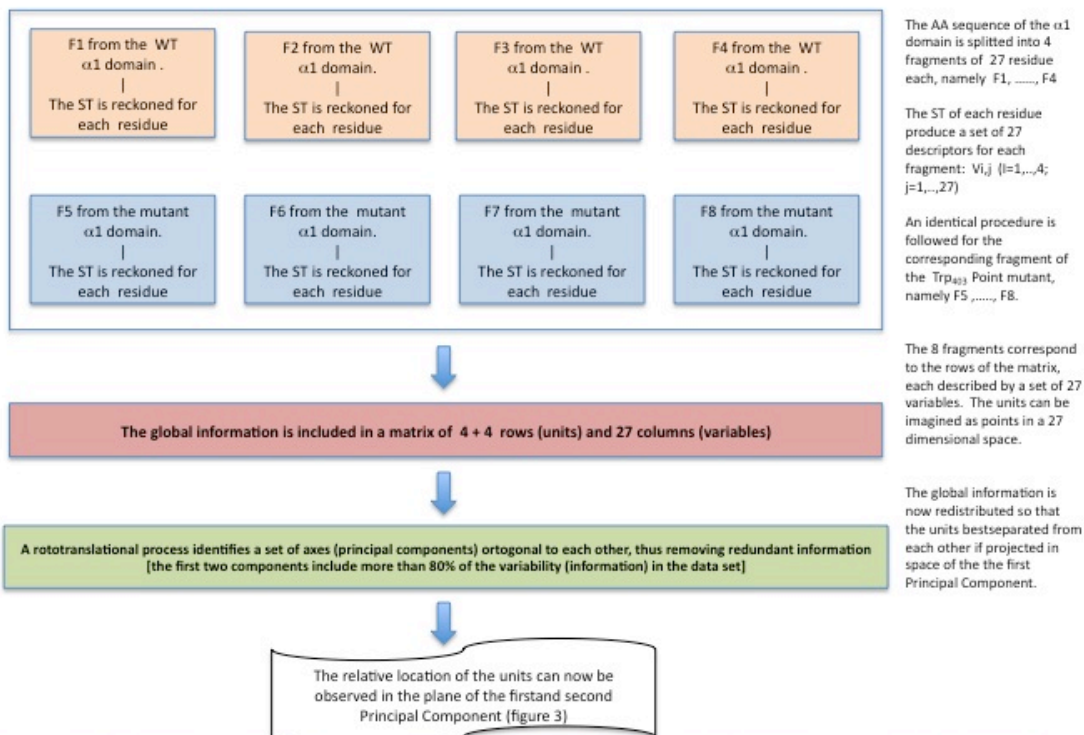
Acknowledgment

References

- Alanen H.I., Salo K.E., Pekkala M., Siekkinen H.M., Pirneskoski A. & Ruddock L.W., Defining the domain boundaries of the human protein disulfide isomerases. Antioxid Redox Signal 5, 367–374, 2003.
- Antal M.A., Böde C., and Csermely P., Perturbation waves in proteins and protein networks: applications of percolation and game theories in signaling and drug design. Curr Protein Pept Sci, 10:161–172, 2009.
- Cai H., Wang C.C. & Tsou C.L., Chaperone-like activity of protein disulfide isomerase in the refolding of a protein with no disulfide bonds. J Biol Chem 269, 24550–24552, 1994.
- De Almeida R.M.C., Lemke N., Jund P., Jullien R., and Campbell I.A. et al., Dynamics of complex systems above the glass temperature. J. Non-Cryst. Solids, 287:201–209, 2001.
- Doncheva N.T., Klein K., Domingues F.S., and Albrecht M., Analyzing and visualizing residue networks of protein structures. Trends in Biochemical Sciences, 36:179–182, 2011.
- Frickel E.M., Frei P., Bouvier M., Stafford W.F., Helenius A., Glockshuber R., Ellgaard L., ERp57 is a multifunctional thiol-disulfide oxidoreductase J Biol Chem. 2004 Apr 30;279(18):18277-87, 2004.
- Goldberger R.F., Epstein C.J. & Anfinsen C.B., Purification and properties of a microsomal enzyme system catalyzing the reactivation of reduced ribonuclease and lysozyme. J Biol Chem 239, 1406–1410, 1964.
- Jackson, J.E., A User's Guide to Principal Components (Wiley), 1991.
- Maslov S. and Ispolatov I., Propagation of large concentration changes in reversible protein-binding networks. Biochemistry, 104:13655–13660, 2007.
- McLaughlin S.H. & Bulleid N.J., Thiol-independent interaction of protein disulphide isomerase with type X collagen during intra-cellular folding and assembly. Biochem J 331, 793–800, 1998.
- Smoot M., Keiichiro O., Ruscheinski J., Wang P.L., and Ideker T., Cytoscape 2.8: new features for data integration and network visualization. Bioinformatics,, 27(3):431–432, 2011.
- Szalay, K. Z. and Csermely, P., Perturbation centrality and Turbine: A novel centrality measure obtained using a versatile network dynamics tool. PLoS ONE, 8, e78059, 2013.
- Turano C., Coppari S., Altieri F. and Ferraro A., Proteins of the PDI Family: Unpredicted Non-ER Locations and Functions J. Cell. Physiol., 193, pp. 154–163, 2002
- Zhong Q., Simonis N., Li Q.R., Charloteaux B. and Heuze F. et al., Edgetic perturbation models of human inherited disorders. Mol. Syst. Biol., 5:321, 2009.

Appendix A: How to draw Figure 2 in the text

Ala$_{403}$ (WT)　　　　　　　**Trp$_{403}$ (Mutant)**

Left and Right panels: location in the 3D structure, of Ala$_{403}$ (WT) and of Trp$_{403}$ (Point Mutant), respectively.

1) Each residue is excited by an energy input;
   (energy dissipates throughout the whole molecule)
2) The SILENCING TIME is recorded for each residue
   and averaged over the whole sequence

1) A profile of silencing times is thus obtained for the WT sequence
   as well as for the mutant sequence
2) The two profiles are compared and the difference at the level of single
   residues, calculated in terms of fractional change
   with respect to the wild type: (WT – M) / WT.

The difference between WT and mutant forms reflecting the influence of both location and substituted residues, can be included in a single plot(Figure 2)

Appendix B: A Principal Component Analysis of silencing times in the WT and a' domain of ERp57.

F1 from the WT α1 domain.	F2 from the WT α1 domain.	F3 from the WT α1 domain.	F4 from the WT α1 domain.
The ST is reckoned for each residue	The ST is reckoned for each residue	The ST is reckoned for each residue	The ST is reckoned for each residue

F5 from the mutant α1 domain.	F6 from the mutant α1 domain.	F7 from the mutant α1 domain.	F8 from the mutant α1 domain.
The ST is reckoned for each residue	The ST is reckoned for each residue	The ST is reckoned for each residue	The ST is reckoned for each residue

The AA sequence of the α1 domain is splitted into 4 fragments of 27 residue each, namely F1, ..., F4

The ST of each residue produce a set of 27 descriptors for each fragment: $V_{i,j}$ (I=1,...,4; j=1,...,27)

An identical procedure is followed for the corresponding fragment of the Trp$_{403}$ Point mutant, namely F5 ,......, F8.

The global information is included in a matrix of 4 + 4 rows (units) and 27 columns (variables)

The 8 fragments correspond to the rows of the matrix, each described by a set of 27 variables. The units can be imagined as points in a 27 dimensional space.

A rototranslational process identifies a set of axes (principal components) ortogonal to each other, thus removing redundant information (the first two components include more than 80% of the variability (information) in the data set)

The global information is now redistributed so that the units best separated from each other if projected in space of the the first Principal Component.

The relative location of the units can now be observed in the plane of the firstand second Principal Component (figure 3)

Legend: AA = AminoAcid ; ST = Silencing Times

Protein Translocation through Nanopores: Insights from Computational and Theoretical approaches

Mauro Chinappi[a], Emma Letizia Bonome[b], Tudor Luchian[c], Fabio Cecconi[d*]

[a] CLNS@Sapienza, Istituto Italiano di Tecnologia, Via Regina Elena 291, 00171, Roma, Italia
[b], Univerisità di Roma La Sapienza, Via Eudossiana 18, 00184, Roma, Italia
[c] CNR-Istituto dei Sistemi Complessi UoS "Sapienza," Via dei Taurini 19, 00185 Roma, Italia
[d] Department of Physics, Laboratory of Molecular Biophysics and Medical Physics, Alexandru I. Cuza University, Iasi 700506, Romania

Abstract

Voltage driven translocation in nanopores is a promising experimental technique capable of inferring the physical chemical properties of the passing molecule by the variation of the resistance of the nanopore based devices. The tecnique needs some improvements especially when applied to complex biopolymers like proteins. In this work we discuss some computational and theoretical approaches that allow to characterizing and clarifying some elementary mechanisms, such as molecule capture and transport rates, that constitute the key elements of the working principle of the whole technique. The results we present can suggest some improvement and optimization of the efficiency of nanopore devices for protein sensing.

Keywords: Nanopore Sensing; Co-translocational unfolding; Nanopore tweezer; Simulations.

1. Introduction

During the past two decades, nanopores have been exploited for the development of innovative approaches for DNA sequencing and several research groups have focused their activities on the interpretation of current signals associated with nucleic acid translocation (Mikheyev et al, 2014, Schneider et al., 2010). Much less effort has been devoted to protein and polypeptide sensing and, only in recent years, protein analysis via nanopores has become a massive subject of research with the purpose of suggesting possible applications to sequence and structure analysis (Cressiot et al, 2014, Rodriguez-Larrea and Bayley, 2013, Boynton and Di Ventra, 2015). A typical experimental set-up, Fig 1A, employs the α-Hemolysin (αHL) nanopore, a toxin from Staphylococcus aureus (Song et al. 1996). The sensing site allows the passage of only one monomer, while the vestibule has enough room for accommodating secondary structure elements and partially folded chains that can give raise to a multilevel current signal, Fig 1B.

The uniform charge of polynucleotides (nucleic acid) makes their electrophoretic translocation in nanopore relatively easy and regular, on the contrary, polypeptides (proteins), being not uniformly charged polymers, translocate in complex pathways. In addition, the not uniform charge cannot allow a fine control of the translocation rates by tuning the electric field intensity. This issue affects directly the sensitivity of a nanopore device; a good sensitivity requires that just one residue at a time has to occupy the pore sensing site and that the residence time has to be long enough to record a stable current signal. Finally, proteins, unlike DNA, spontaneously assume compact native conformations and their passage in nanopores is possible only when accompanied to unfolding. All these issues pose a great challenge in developing reliable sensing nanopore devices for proteins and peptides.

In the present proceeding, we briefly discuss our recent theoretical and computational approaches aimed at controlling the translocation rate and unravel the complex pathway associated to protein translocation.

2. Characterization of co-translocational unfolding

As mentioned in the introduction, a crucial issue in nanopore protein sensing is the achievement of protein capture and the control of translocation rates. Oukhaled et al., 2007, studies the translocation of the Maltose Binding Protein, that at physiological pH has a net charge such that electrophoretic transport is possible. The same happens also for certain peptides studied by Mereuta et al., 2014. However, in both cases, the chains need to be completely unfolded before the translocation starts. This results in a very high translocation rate that gives rise to flat current signals that do not resolve nature of the translocating residues. A crucial improvement in this respect was achieved in 2013, when two different groups proposed a novel strategy to control protein translocation by adding a charged linker to one of the two termini of the molecule to be analyzed, Nivala et al., 2013 and Rodriguez-Larrea and Bayley, 2013. In particular, this

second set-up allowed, for the first time, to measure a multistep current signal associated with the transport of a protein inside a nanopore.

In the above cited experiments, the only accessible information on the nanopore-macromolecule interaction is the current signal. Hence, the interpretation of the actual translocation pathway relies on both the indirect evidences extracted from the current behaviour and on a wide number of tests that involves designed mutants (for instance deleting portion of the peptide or destabilizing specific regions). Simulations have the possibility to provide a molecular level description of the process.

On atomic scale simulations are extremely informative about the protein microscopic dynamics, as they take into account the finer details of structures and interactions. Although the high complexity of the systems prevents atomic-scale simulations from cumulating a necessary number of events for a meaningful statistical mechanical description, the current computational resources allow to reproduce quite accurately the experimental systems. Concerning the translocation of thioredoxin (Trx) we analyzed the process both in αHL pore and in a graphene pore the diameter of which is similar to the αHL sensing site, see Bonome et al., 2015 and Di Marino et al., 2015.

In the simulation protocols, we induce the protein translocation applying a constant force to its C-terminal, see Bonome et al 2015. The resulting pathway shows a not uniform translocation where the proteins "stall" at specific and quite reproducible conformations. Right panels of Fig 2 report the time evolution of the number of untranslocated amino acids Np (108 indicates the initial condition where the whole protein is untranslocated, while 0 means that the whole protein has translocated) for two replicas of the pulling protocol. The main stalls, appearing as plateaus in the Np curves, are associated with the pore "clogged" by more than one amino acid, i.e. not only by the translocating amino acid but also by the portion of the untranslocated region of the chain. The Trx translocation is hence characterized by two main stages. In the early stage the protein gradually unfolds and only one residue occupies the pore. The passage of the central β-strand of the Trx β-sheet (β3 in the left panels of fig. 2) destroys the native fold and also drags with itself part of the untranslocated structure at the pore mouth. This pathway results in several rearrangements of the Trx generating various stalls (plateaus in Np curves). All of them correspond to conformations where amino acids originally belonging to β2 occupy the pore. Interestingly, the different stalls are associated to different ionic currents and, in particular, the pore-clogging conformations result in greater current reductions, allowing to speculate on the possible causes of the multistep signal observed in experiments. A similar co-translocational unfolding pathway was also observed for Trx translocation through αHL pore (Di Marino et al., 2015).
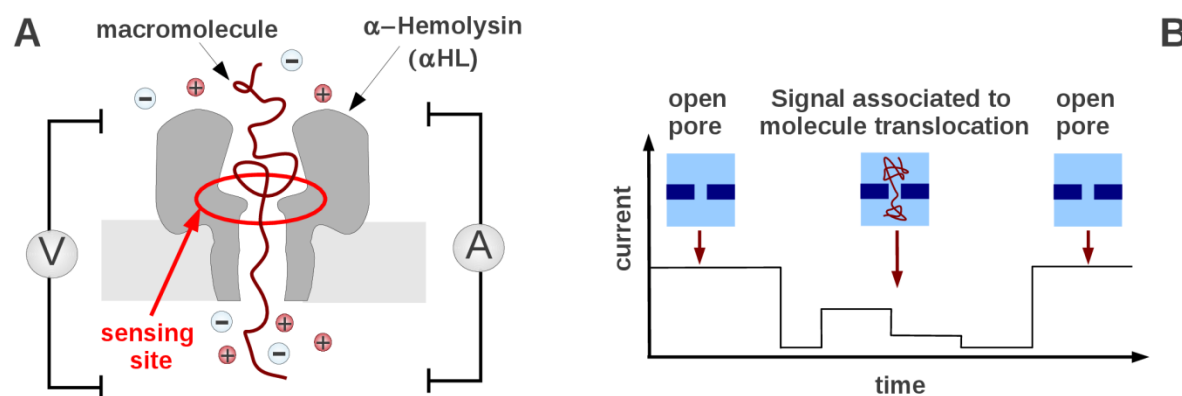

Figure 1: Nanopore sensing principle. Panel A) A nanopore is embedded in a membrane. When a voltage is applied between the two chambers (V in panel A) a ionic flux sets in. This ionic flux can be easily measured using an amperometer (A in panel A). The presence of a molecule inside the pore results in an alteration of the current. The reduction in the conductance is due to the conformation of the macromolecules inside the pore however, the main contribution comes from the narrowest section (sensing site). In the case of α-Hemolysin (αHL), the constriction is 1.4 nm in diameter and it allows the passage of only a single residue (panel A). Panel B reports a sketch of a possible multistep current signal associated to the passage of a protein that unfolds during the translocation process (co-translocational unfolding).

3. Peptide trapping

A second crucial issue in nanopore protein and peptide sensing is the control of the translocation rate. In this respect is was recently show that the addition of a positive and a negative tail to a neutral peptide, increases the residence time of the molecule inside the nanopore, Asandei et al., 2015. We shortly discuss the fundamental mechanism behind the trapping of peptides by the pore. The applied potential ΔV induces a non-homogeneous electrical field that is more intense inside the nanopore. The artificial polarity of the molecule favors its capture since the dipole tends to orient along the field lines that converge into the pore axis, Fig 3a. Indeed, as long as the molecule enters the pore, it experiences an increasing importing force due to the larger electrical field, Fig 3b. When also the other charged tail

engages the pore, an opposite couple of forces generates a sort of "tug-of-war" for which the analyte becomes stably trapped in the pore center, Fig 3c and 3d. Since the intensity of the electrical field can be controlled by changing the voltage ΔV, both capture and escape rates can be easily tuned. In particular, the capture rate increases with voltage while the escape rate decreases. In a recent work (Chinappi et al, 2015), we recasted this phenomenological interpretation in a more rigorous approach based on the estimation of the free-energy barriers associated to the translocations. Sketches of the model system and of the free-energy profile are reported in figure 3e and 3f. The particle has to overcome a capture barrier to enter the pore (due to entropic cost of the confinement), once it is inside the pore it gets trapped in the minimum of the free-energy and it has to pay a further free-energy cost to escape. The escape and the capture barrier depend on the applied potential ΔV. In particular, escape barrier increases with ΔV, realizing the trapping mechanism. Remarkably, this approach, dubbed nanopore tweezer, is not limited to macromolecules but, in principle, can work also at larger scales, since the only ingredients are the nonhomogeneous electrical field induced by the nanopore in presence of an applied voltage ΔV and a particle with high dipole moment.
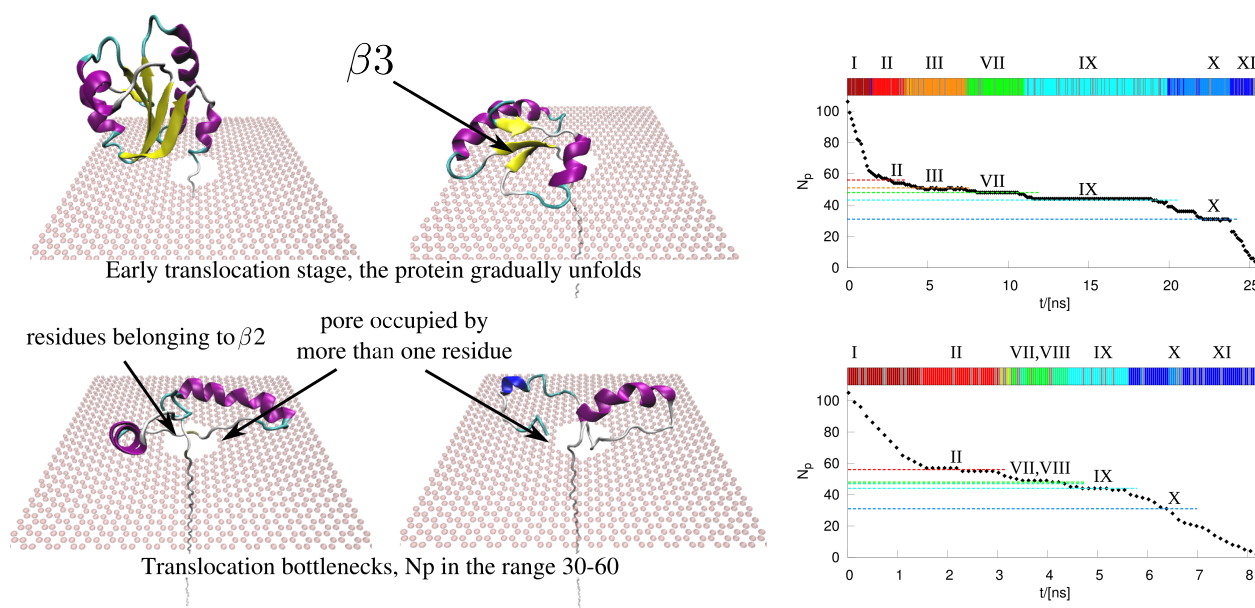

Fig 2. Multistep translocation pathway of Thioredoxin through a graphene nanopore. Left panels show the main phases of the translocation pathway. In the early stage the protein gradually unfolds and only one residue occupies the pore. The passage of the strand β3 of the thioredoxin β-sheet destroys the native fold and drags part of the untranslocated structure at the pore mouth. This results in several rearrangements of the thioredoxin that give raise to various stalls (plateaus in Np curves indicated via roman digit in the right panels). Right panels were obtained using VMD, (Humphrey et al 1996), while the simulations where performed using NAMD, Phillips et al 2015.
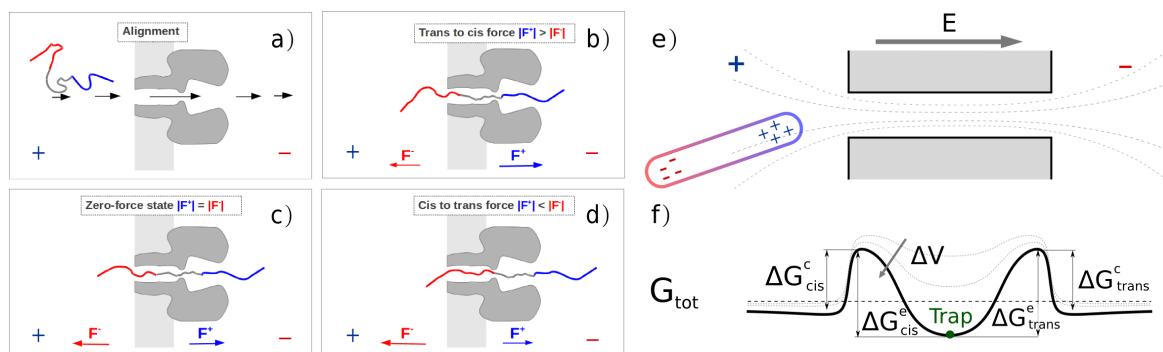

Figure 3. Nanopore tweezer. a) The applied voltage results in an inhomogeneous electrical field that is larger inside the nanopore. The field aligns the peptide with the positive tail towards the pore mouth. b) The resulting electrostatic force drives the polypeptide into the pore. As the positive residues exit from the pore side and negative residues enters, |F+| decreases while |F-| increases until the two forces approximately balance (zero net force

stage, panel c). Further movements of the polypeptide towards the positive (b) or the negative electrode (d) result in an electrical force that drives the peptide back to the zero force state, Asandei et al, 2015. Panel e and f report the interpretation of the tweezer principle in terms of free-energy barriers, Chinappi et al 2015.

4. Future developments

Both the results briefly presented here are associated to experimental set-ups where specific modifications of the peptide chain termini are needed. In this respect, recent experimental developments in manipulating the peptide structure, such as the "click" reaction proposed by Biswas et al, 2015, can potential pave the way to a more systematic employment of the discussed approaches. On the computational side, it is nowadays relatively easy to completely reproduce the nanopore experimental systems in full details (Belkin et al, 2015), although ad hoc protocols have to be employed to induce the translocation on accessible time scales. This allows to numerically test theoretical ideas and to have an immediate interpretation of the experimental results in terms of specific peptide conformations occupying the pore sensing regions.

Acknowledgements

References

Mikheyev, Alexander S., and Mandy MY Tin. "A first look at the Oxford Nanopore MinION sequencer." Molecular ecology resources 14.6 (2014)

Schneider, G. F., Kowalczyk, S. W., Calado, V. E., Pandraud, G., Zandbergen, H. W., Vandersypen, L. M., & Dekker, C. (2010). DNA translocation through graphene nanopores. *Nano letters*, *10*(8), 3163-3167.

Rodriguez-Larrea, D., & Bayley, H. (2013). Multistep protein unfolding during nanopore translocation. *Nature nanotechnology*, *8*(4), 288-295.

Song, L., Hobaugh, M. R., Shustak, C., Cheley, S., Bayley, H., & Gouaux, J. E. (1996). Structure of staphylococcal α-hemolysin, a heptameric transmembrane pore. *Science*, *274*(5294), 1859-1865.

Cressiot, B., Oukhaled, A., Bacri, L., & Pelta, J. (2014). Focus on protein unfolding through nanopores. *BioNanoScience*, *4*(2), 111-118.

P. Boynton and M. Di Ventra, "Sequencing proteins with transverse ionic transport in nanochannels", arXiv:1509.04772v1

Oukhaled, G., Mathe, J., Biance, A. L., Bacri, L., Betton, J. M., Lairez, D., ... & Auvray, L. (2007). Unfolding of proteins and long transient conformations detected by single nanopore recording. *Physical review letters*, *98*(15), 158101.

Mereuta, L., Roy, M., Asandei, A., Lee, J. K., Park, Y., Andricioaei, I., & Luchian, T. (2014). Slowing down single-molecule trafficking through a protein nanopore reveals intermediates for peptide translocation. *Scientific reports*, *4*.

Nivala, Jeff, Douglas B. Marks, and Mark Akeson. "Unfoldase-mediated protein translocation through an [alpha]-hemolysin nanopore." *Nature biotechnology* 31.3 (2013): 247-250.

Bonome, E. L., Lepore, R., Raimondo, D., Cecconi, F., Tramontano, A., & Chinappi, M. (2015). Multistep Current Signal in Protein Translocation through Graphene Nanopores. *The Journal of Physical Chemistry B*, *119*(18), 5815-5823.

Di Marino, D., Bonome, E. L., Tramontano, A., & Chinappi, M. (2015). All-Atom Molecular Dynamics Simulation of Protein Translocation through an α-Hemolysin Nanopore. *The journal of physical chemistry letters*, *6*(15), 2963-2968.

Asandei, A., Chinappi, M., Lee, J. K., Seo, C. H., Mereuta, L., Park, Y., & Luchian, T. (2015). Placement of oppositely charged aminoacids at a polypeptide termini determines the voltage-controlled braking of polymer transport through nanometer-scale pores. *Scientific reports*, *5*.

Asandei, A., Chinappi, M., Kang, H. K., Seo, C. H., Mereuta, L., Park, Y., & Luchian, T. (2015). Acidity-Mediated, Electrostatic Tuning of Asymmetrically Charged Peptides Interactions with Protein Nanopores. *ACS applied materials & interfaces*, *7*(30), 16706-16714.

Chinappi, M., Luchian, T., & Cecconi, F. (2015). Nanopore tweezers: Voltage-controlled trapping and releasing of analytes. *Physical Review E*, *92*(3), 032714.

Biswas, S., Song, W., Borges, C., Lindsay, S., & Zhang, P. (2015). Click Addition of a DNA Thread to the N-Termini of Peptides for Their Translocation through Solid-State Nanopores. *ACS nano*, *9*(10), 9652-9664.

Belkin, M., Chao, S. H., Jonsson, M. P., Dekker, C., & Aksimentiev, A. (2015). Plasmonic Nanopores for Trapping, Controlling Displacement, and Sequencing of DNA. *ACS nano*.

Humphrey, William, Andrew Dalke, and Klaus Schulten. "VMD: visual molecular dynamics." Journal of molecular graphics 14.1 (1996): 33-38.

.

Neural newtwork mechanisms simulated by Multi Agent Systems.
Alfredo Colosimo

Dept. S.A.I.M.L.A.L. – Sapienza University of Rome

Abstract

By focusing on standard parameters from the Graph Theory, like the Average Path Length and the Clustering Coefficient, one may connect the arrangement of topological/physical links in Artificial Neural Networks (ANN) to the networks' functional properties. Taking advantage of that, simulations based on a Multi Agent Systems (MAS) were used to study the response to asymmetric, random stimuli in neural populations. We could show that **in** small networks even single, local changes in the link pattern induce significant alterations in global functional parameters. In addition, it seems fair to state that using negative values for links' weights, although requiring uncommon software tools, is a great enhancement of ANN euristic power in a number of practical applications.

Keywords: Artificial Neural Networks; Dynamical Simulations; Multi Agent Systems; Negative Links' Weights.

Introduction

From the Adiacency Matrix (AM) of the graph associated to a network of N nodes, the Average Path Length (APL) and the Clustering Coefficient (CC) were introduced as topological parameters characterizing the 'small word' properties of the network at hand [Watts and Strogatz, 1998]. In the binary version of the matrix, using 0/1 values for the a_{ij} entry (for $\forall i \neq j$) indicates the presence or absence of a link (edge) connecting nodes *i and j*. The use of real numbers $\{l_{ij}\}$, however, allows to extend the interpretation of links in terms of physical distances [Latora and Marchiori, 2001], and of cost/efficiency considerations. In that case, the APL (topological) parameter switches to its physical counterpart APD (Average Physical Distance). Figure 1 shows two different edge patterns for a 9-node network together with the associated parameters.
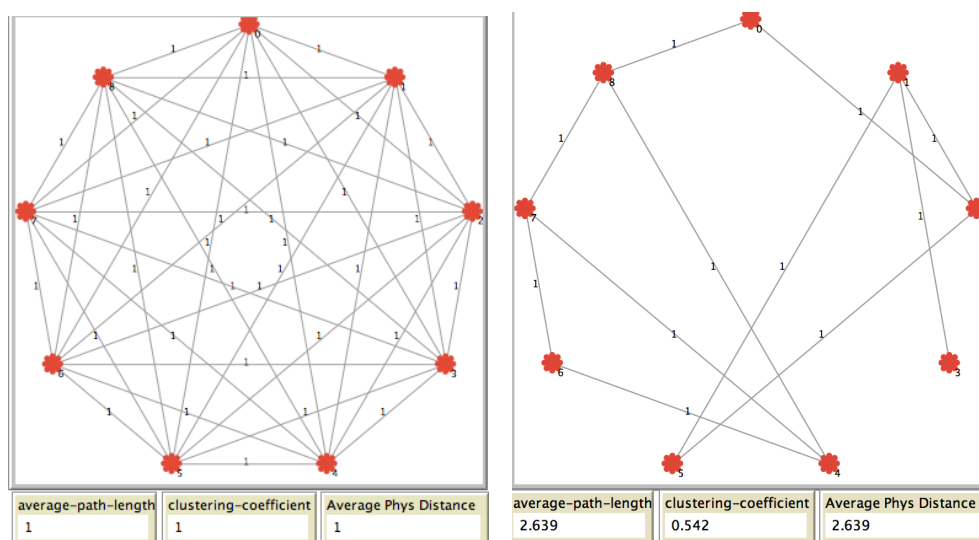

average-path-length	clustering-coefficient	Average Phys Distance
1	1	1

average-path-length	clustering-coefficient	Average Phys Distance
2.639	0.542	2.639

Figure 1. Topological and physical parameters in a 9-node network.
Left: Fully connected network (36 links). Right: Partially connected network (11 links). APL and APD (see also Appendix a) are averages of, respectively, the *Shortest Path Length* (SPL) and *Shortest Physical Distance* (SPD). Notice that cutting any of the 36 (topologically equivalent) links in the left, highly symmetric network, both APL and APD increase to 1.028, while after increasing the weight of one (or more) link in the right, highly asymmetric network, only the APD increases (see Figure 2B).
The pictures have been obtained by an original routine written in the Netlogo environment [Wilenski, 1999].

In the case of full connectivity (Figure 1, left) the APL and APD are both unitary. After

relaxing the full connectivity condition (Figure 1, right) APL and APD still retain the same value but become now sensitive – although at different rates - to changes in the links' weight and location. Figure 2 clarifies the point : in Figure 2(A) the location and weight of the edges are kept the same as in Figure 1(Right); in the (B) panel the $N_0 \leftrightarrow N_8$ weight is increased by 20 times as compared to (A) and, in the (C), the $N_0 \leftrightarrow N_8$ and the $N_0 \leftrightarrow N_4$ edges are swapped as compared to (B).
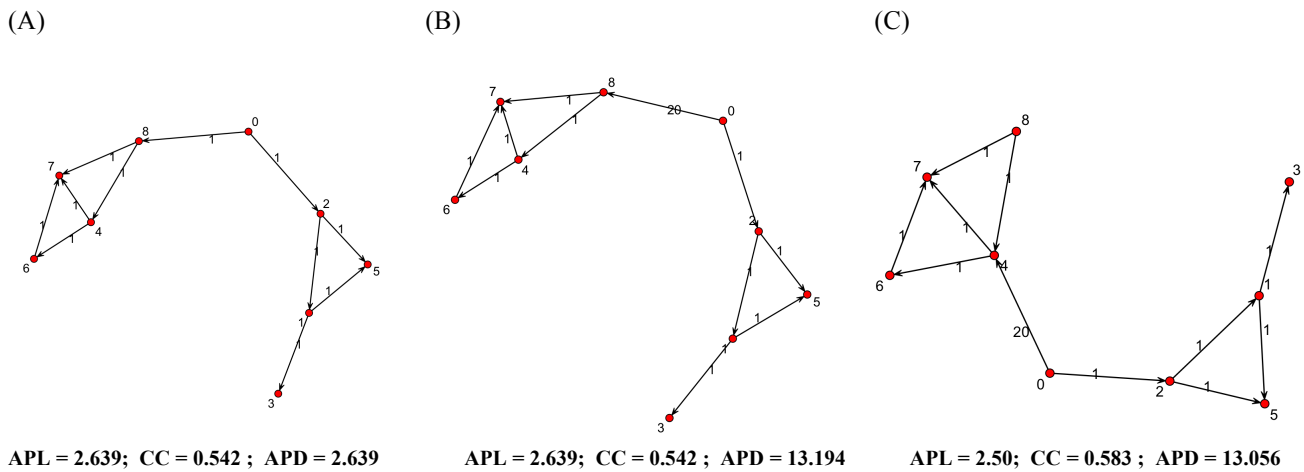
(A)   (B)   (C)

APL = 2.639; CC = 0.542 ; APD = 2.639   APL = 2.639; CC = 0.542 ; APD = 13.194   APL = 2.50; CC = 0.583 ; APD = 13.056

Figure 2. *Sensitivity of network parameters to topological and physical link patterns.*
The pictures have been obtained by Adjacency Matrices (see Appendix b) worked out in the Netlogo programming environment [Wilenski, 1999] and subsequently imported into R 3.2.1 [R Foundation] for further manipulation and graphical output.

Thus, in panel (A) of Figure 2 the APL, CC and APD values remain unchanged with reference to Figure 1(Right), while in panel (B) the the APD (Average Physical Distance) is changed due to the weight change in the $N_0 \leftrightarrow N_8$ edge. As expected, in the (C) panel all of the three parameters change at a larger extent with reference to panel (A) than to panel (B): only in the former case, in fact, both weight and location of the $N_0 \leftrightarrow N_8$ edge did change.

Results.

1) Exploiting the combined use of different software tools in modeling networks' functions.

Figure 3 contains the same 9-node network introduced in Figure 2 using the representation provided by Mathematica^{TM}. The aim is to take advantage of a specific *Mathematica^{TM} extension* available in Netlogo in order to transfer the adjacency matrices generated by Netlogo into Mathematica, for a deeper inspection of network structures. As a first step we decided to reproduce the effect of changing the weight of specific edges on the measure of global, Average Physical Distances (APD) as well as on the tracing of local, Shortest Paths.
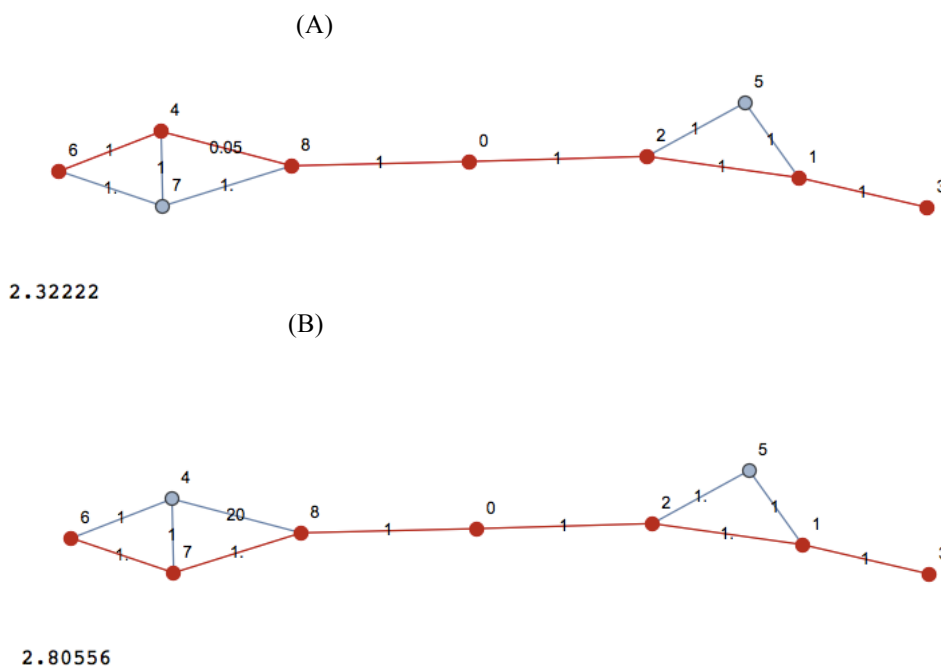
(A)

2.32222

(B)

2.80556

Figure 3. *Single Shortest Paths and APD values in a 9-node net.*
The shortest path between N_3 and N_6 is indicated by the red-colored nodes; APD values are in the bottom left corner of each panel. The pictures have been obtained by a specific Netlogo extension coupled to Mathematica^{TM},

Panels (A) and (B) show the effect on the APL values of decreasing and increasing by the same factor the unitary weight of the N4$\leftrightarrow$N8 link.

(C)
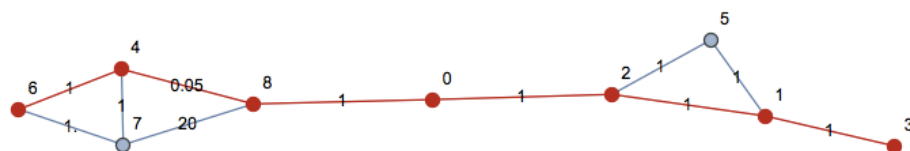
In panel (C)) both changes have been introduced in the two highly symmetric $N_4 \leftrightarrow N_8$ and $N_7 \leftrightarrow N_8$ to check the presence of combined effects.

2.33056

Panels (A) and (B) of Figure 3 show, respectively, the effect on the APL values (indicated on the bottom left corner) of decreasing and increasing by a factor 20 the unitary weight of the $N4 \leftrightarrow N8$ link. Such values are only slightly different from the 2.639 obtained in the reference (Figure 2 (A)), since they are average values and indicate the "dilution" of the weight change over the whole net. It is worth to underline the absence of compensation observed upon increasing the $N_4 \leftrightarrow N_8$ weight and decreasing, at the same time, its symmetric counterpart $N_7 \leftrightarrow N_8$: the APL value in panel (C) is pretty similar to that in (B) since the shortest pathways to be averaged will go, in any case, through the steps endowed with shorter distance (lower energy).

2)   Exploring the effects of negative weights.

The Mathematica^{TM} environment allows to measure APL even in presence of negative weights, through the BellmanFord algorithm [Sedgewick R., 2002] , the reference value remaining that of Figure 1 Right, 2.639 , when all edges = 1 .
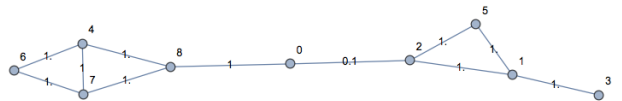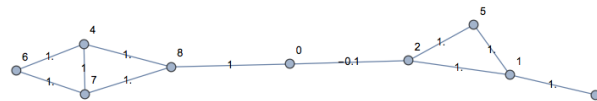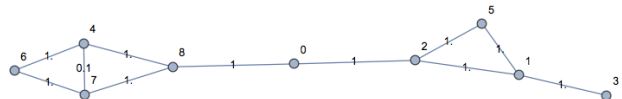
(A)
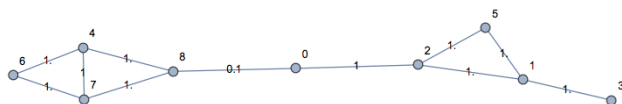
2.13889

(B)

1.73056
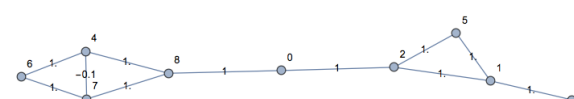
(C)

2.13889

(D)

1.69167

(E)

2.61389

(F)

2.36389

Figure 4   Relative importance of negative and positive weights of specific edges.
Pictures and calculations have been obtained by Mathematica^{TM} V. 10.0 where it is possible to invoke (see Appendix c), the BellmanFord algorithm in order to evaluate – in spite of some limitation - net parameters even in presence of negative weights.

In Figure 4 three couples (A) - (B) , (C) - (D) , (E) – (F) refer to different locations of weight edges of different sign. In all

cases the negative sign induced a significant decrease in APL which is, however, of different size in (B) and (D) while the corresponding positive counterparts (A) and (C), concerning similar but not identical topologies, remain the same. This indicates a noticeable sensitivity of negative weights to even subtle differences in the surrounding edge patterns. Such higher sensitivity also appears when the location is confined to relatively peripheral location, as in the (E) – (F) couple. According to Sedgewick [Sedgewick R., 2002] the negative weights of a nets' edge are naturally present when dealing systematically with *minimun path* problems [Sedgewick R., 2002]. In the present context the issue becomes relevant if considered in conjuction with some pathophysiological models in neuroscience (see below).

Discussion

The recognized ability of the Netlogo [Wilenski, 1999] MAS programming environment in the reproduction of complex population dynamics revealed helpful also in exploring the global effects of localized structural changes within the node/edge pattern of artificial networks. It is difficult to overestimate the benefit of combining the specific virtues of Netlogo with those of other programs, like R-Statistical Software or Mathematica^{TM}, more flexible in dealing with graphical output or sophisticated algorithms. We took advantage of that to study a minimalistic 9-node network still endowed with interesting features, like two similar but not identical sub-networks connected through a single node [Figures 1, Right].

In small networks changing the weight or position of a few (or even single) edges induces alterations in global parameters related to functional properties like APL, CC and APD. As expected, APL and CC showed particularly sensitive to edges' location, while APD was mainly influenced by the pattern of weights [Figure 2]. By changing the location/weight of edges and visualizing the shortest pathway between distant nodes, one may grasp the ensuing non additive effects on the global, average measures (Figures 3].

Particular attention deserve the effects of tuning to negative values the edge weight in different locations, as shown in Figure 4. Quite interesting appears the APL difference in panels (B) and (D), induced by small, negative weights (- 0.1) in $N_0 \leftrightarrow N_8$ and $N_0 \leftrightarrow N_2$, two almost identical edges from the topological viewpoint, since the positive value (+ 0.1) does not produce any difference between the corresponding panels (A) and (C).

As a matter of fact, a neural source of negative functional connectivity [Keller et al. 2013] has been claimed in the attempt to rationalize the observed pattern of anticorrelation between the activation of some cerebral areas and several physiological and biological variables like caffeine intake, meditation and aging [Chai et al. 2014]. In this perspective, the peculiarity of negative brain network has been observed also in schizophrenic patients [Parente et al, in preparation].

Conclusions

Although dealing with an extreme oversimplification, just a toy-model, of the real neural networks, it is quite suggestive to assimilate the subnetworks on the left and right side of N_0 in Fig. 4 to some real brain areas sharing a common hub. In such a context it could be envisaged that a global, functional measure (APL), is more significantly depressed - or negatively regulated - with respect to a reference, by negative signals running through only one out of two almost identical pathways.

No doubt that positive and negative couplings within and between different (sub)networks, pointing to reproduce stability properties, synchronized functional oscillations and productive randomic events, as considered by several authors with no biological committment (see, for instance Gade and Rangarajan, (2013) and reference therein) appear extremely attractive from a Neurophysiological point of view. On the other hand, in spite of its attractive features, any modelistic approach to mutual regulation between brain areas including negative, deactivating signals, is characterized by a large number of caveats, stemming from the necessary oversimplification or ignorance of the underlying physiological mechanisms.

In any case, to substantial improvements would lead, in our opinion, including the time dimension in the modeling strategies considered in this contribution, by systematic consideration of dynamical phenomena: in such a perspective the use of simulation environments of the MAS type could reveal quite efficient.

REFERENCES

Bullmore, E., and Sporns, O., 2009. Nat Rev Neurosci., 10(3), p. 186.
Chai X.J., Ofen N., Gabrieli J.D. Ana Whitfield-Gabrieli S., 2014, *J. Cogn Neurosci.,* 26(3), p. 501
Colosimo, A., 2008, Biophysics and Bioengineering Letters, 1(3), p. 40.
Colosimo, A., 2011, Biophysics and Bioengineering Letters, 4(2), p. 34.
Gade P.M. and Rangarajan G., 2013, Chaos, 23(3)
Keller C.J., Bickel S. Honey C.J., et al, 2013, *J. Neuroscience*, 33(15), p. 6333
Latora V., Marchiori M., 2001, Phys Rev Lett., 87(19).
R Foundation for Statistical Software (http://www.R-project.org)
Sedgewick R., 2002 "Negative Edge Weights". *Algorithms in Java* (3rd ed.). ISBN 0-201-36121-3.
Watts D., J. and Strogatz, S.,H., 1998, Nature, 393, p.440.
Wilenski, U. , 1999, http://ccl.northwestern.edu/netlogo/

Appendix.

a) Definition of the network parameters used in this work.

Ki = Node Degree *: number of links of node i. In *directed networks* where each link has a selected direction, K_{in} denotes the number of links that point to a node, and K_{out} , denotes the number of links that start from it.
SPL_{ij} = minimum number of links between nodes i and j*;*
APL = Average Path Length = $< SPL >$ over all pairs of nodes.
CC_i = Clustering Coefficient of node i = $2e_i / K_i(K_i - 1$, where e_i = number of connected pairs within the first neighbors of node i
$< cc >$ = average over all nodes having $K > 1$.

b) Adiacency Matrices (in the form of distance matrices) for the nets in Figure 2.

Panel (A)

	N_1	N_2	N_3	N_4	N_4	N_5	N_6	N_7	N_8
N_0	0								
N_1	2	0							
N_2	1	1	0						
N_3	3	1	2	0					
N_4	2	4	3	5	0				
N_5	2	1	1	2	4	0			
N_6	3	5	4	6	1	5	0		
N_7	2	4	3	5	1	4	1	0	
N_8	1	3	2	4	1	3	2	1	0

Panel (C)

	N_0	N_1	N_2	N_3	N_4	N_5	N_6	N_7	N_8
N_0	0								
N_1	2	0							
N_2	1	1	0						
N_3	3	1	2	0					
N_4	20	22	21	23	0				
N_5	2	1	1	2	22	0			
N_6	21	23	22	24	1	23	0		
N_7	21	23	22	24	1	23	1	0	
N_8	21	23	22	24	1	23	2	1	0

c) Mathematica commands producing Figure 4

```
<<NetLogo` NLStart[]                        #  Activates the Netlogo connection

NLLoadModel[…… SimpleCopy03.nlogo"]]        #  Loads the Netlogo program for network generation

network=NLGetGraph["links"]                 #  Translates from Netlogo the features of the
weights=NLReport["[label] of links"]        #  specific network at hand

GraphPlot[network]                          #  Draws the network backbone


weights                                     # Lists the edge weights before and after
weights[[2]] = -0.1;                        # arbitrary changes
weights                                     # (in arbitrary number)

####  combination of (gg1) and (gg2) draws the network including nodes and edge labels.

gg1=Graph[network,EdgeWeight--> weights,VertexLabels-->"Name",EdgeLabels-->
        Table[network[[i]]weights[[i]],{i,Length[network]}],DirectedEdges -> False] ;
gg2=HighlightGraph[gg1,PathGraph@FindShortestPath[%,6,3,Method-> "BellmanFord"]]

MeanGraphDistance[gg1]                       # reckons the APL value  for the network at hand
```

Implementation of a 3D Printing Software for renal anatomical structures

Frazzetta G[a], Felici A[a], Miano R[b], Nezzo M[c], Germani S[b], Abundo P[a], Manenti G[c], Vespasiani G[b], Rosato N[a]

[a]Medical Engineering Service, Fondazione Policlinico Tor Vergata, Rome, Italy
[b]Experimental Medicine and Surgery dept, Fondazione Policlinico Tor Vergata, Rome, Italy
[c]Diagnostic Imaging and Interventional Radiology, Fondazione Policlinico Tor Vergata, Rome, Italy

Abstract

3D printing is a fast growing and developing production technology. Medical field is among those that can benefit the most from this technology, as medical devices usually require high customization, fast availability and a variety of possible materials. Among various medical applications, the production of 3D printed medical models is an active field of studies, because they can provide clinicians with the opportunity to plan, test and practice surgical procedures on an exact replica of the body part involved before the actual procedure takes place.

While many renal surgical procedures are well established and developed, each kidney's peculiar morphological characteristics must be taken into account. The use of training models and simulators can improve surgeons' dexterity and performances, but currently available models often lack patient-wise customization.

Our study, led in cooperation with the Medical Engineering Service in "Policlinico Tor Vergata" hospital focused on the implementation a software that allows clinicians themselves to extract 3D printable model files from ordinary kidney 4 phase CT (Computed Tomography) studies to be used for the development of a patient-specific renal simulator. The software was revised and tested in the Urology and the Imaging wards in Rome's hospital "Policlinico Tor Vergata", receiving positive feedback from clinicians in terms of anatomical accuracy and usability.

1. Main text

3D printing is quickly gaining attention in a number of medical disciplines. As for Urology, promising studies by Shiga et al [1] and by Bernhard et al. [2] show that 3D printed kidney models can play a major role in tumor identification and removal. The core of this project consists in the implementation of a software that, starting from standard imaging files of a kidney 4 phase CT (Computed tomography) scan, exports a series of 3D printable files of the kidney and its internal structures, such as ureter, vein and arteries, and its surrounding structures, such as bones. The main feature we strove to achieve was to enable clinician themselves to make their own 3D printed model, providing them with a tool they could actually integrate in their daily routine, to get a better understanding of their own cases and patients.

1.1. Software structure

The 3D Kindey Model Making Software is inspired by image processing tools and software commonly used in radiology departments; the aim is to enable physicians themselves to produce printable kidney model files by simple and familiar interaction. The software has been implemented in Matlab®, with the possibility to export it as a standalone application. Other developing solution have been tested and considered, among those the ITK Snap [3] and 3D Slicer suite [4], both of which for new libraries and functions implementation. Even if Matlab® was finally chosen as the main programming suite, ITK Snap and 3D Slicer have proven useful tools in the early stages of the project; 3D Slicer kept on being used throughout the work as immediate mean of results verification and comparison.

The software comprises a main routine that creates the 3D kidney printable files starting from DICOM (Digital Imaging and COmmunications in Medicine) data, and some additional features such as label fast conversion and file review to improve usability and customization.

Figure 1 shows software's structure scheme. Steps requiring user interaction are properly marked.

Fig. 1. Software's structure scheme.
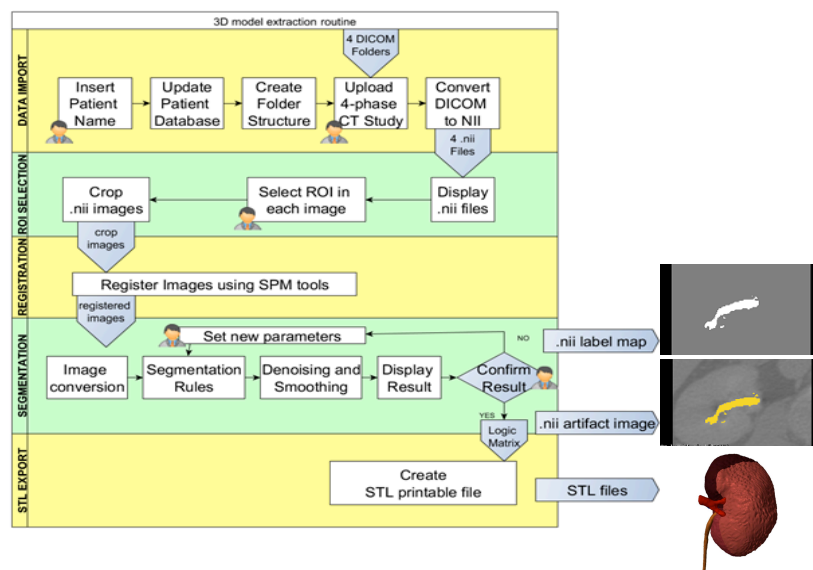
1.2. Input

In order to provide clinicians with a useful tool, the kidney model shall be as much complex and detailed as possible. 4-phase CT studies are a rather common diagnostic tool as they allow collecting a good amount of data about kidney morphology and functionality. A 4-phase CT study consists of four CT scans timed to track an intravascular iodinated contrast media as it flows through kidney arteries, veins and ureter. The routine requires the input of four DICOM series from the same subject with minimal body movement between the acquisitions; the required phases are shown in Table 1.

CT scans are acquired and managed using the DICOM standard. Before processing, DICOM files are converted into the relatively new NIfTI (Neuroimaging Informatics Technology Initiative) format. NIfTI was preferred over DICOM because of the convenience to convert a series of multiple DICOM files in a single .nii file that stores voxels gray values in a tri-dimensional matrix, and because of its peculiar characteristics in terms of image transformations.

Table 1. Input series

Series Name	Software ID name	Post injection acquisition delay (t)*	Contrast media flows in
No contrast phase	No_contrast	Pre-injection	Nowhere
Corticomedullary phase	Arterial	25-50 s	Mainly arteries
Nephrographic phase	Venous	85-120 s	Mainly veins
Excretory phase	Excretory	420-460 s	Mainly ureter and bladder

*timing may vary according to known renal conditions.

1.3. Segmentation of the anatomical structures

The complete segmentation routine consists in three main steps:

- Registration
- Segmentation
- STL conversion

During the examination, that takes about 30 minutes, kidneys can shift or generally move due to the respiratory cycle or some patient's change of position. Image registration is therefore necessary to best match the four NIfTI files, perform a correct data analysis, and to obtain printable part files in the correct relative position. *Registration* is performed using one of the SPM (Statistic Parametric Mapping) suite [5] tools, using the arterial phase as reference image and transforming the remaining 3 phases to match the kidney position. The arterial phase depicts the smallest components to be segmented; choosing it as fixed avoids resampling related data losses. Obviously, SPM main features are not meant to be used in a kidney related environment; nevertheless, SPM preprocessing tools have provided good results performing registration between phases.

The *segmentation* process discriminates different kidney components relying on their different aspect in each of the four phases, due to the contrast mean flow that implies a difference of gray level intensity for the pertinent voxels in each phase. For each kidney component to be segmented, there is a specific segmentation rule with at least one user-controlled parameter. Once the parameter is set, the segmentation is performed and a logic 3D matrix is produced. After some denoising and smoothing steps, the logical matrix is converted in a NIfTI label and combined with the original NIfTI image. The artifact NIfTI image is then show to the user, who can either confirm the result and proceed to the next step or set a new segmentation parameter to get a better result.

The segmentation rules for bone tissue, ureter, renal tissue and vessels are based on the following formulas:

$$[bones\_map] = \begin{cases} 1......[no\_contrast] \geq threshold \\ 0......[no\_contrast] < threshold \end{cases}$$

$$(1)$$

$$[ureter\_map] = \begin{cases} 1......[excretory]-[no\_contrast] \geq threshold \\ 0......[excretory]-[no\_contrast] < threshold \end{cases} \qquad (2)$$

Where square brackets indicate the matricial representation of each dataset and threshold values in (1) and (2) can be set by the user.

$$[kidney\_vess\_map] = \begin{cases} 1......\left|[arterial]-\left(\mu *+offset_1\right)\right| < \sigma \\ 0......\left|[venous]-\left(\nu *+offset_2\right)\right| > \sigma \end{cases} \qquad (3)$$

Where $\mu*$, $\nu*$ are automatically determined analysing the 2D histogram obtained from the arterial and venous series gray level distributions, σ is a fixed value and the offsets can be set by the user to expose both kidney tissue and vessels or either one of them separately.

After user confirmation of the results, label maps identifying the segmented tissues are converted in STL (STereo Lithography interface) format, a standard 3D printing file format and can be post processed and printed.

1.4. Software testing

The software was tested in Policlinico Tor Vergata Urology and Imaging department to assess the anatomical correctness of the extracted STL files and to gather feedback about software reception, usage and performance directly by its potential users. A total of 11 different dataset from anonymous patients were processed; 8 dataset showed healthy kidneys, 2 datasets showed kidney with moderate to severe stones, 1 dataset showed a hydronephrosis condition. The clinicians were asked to evaluate already processed data as well as process data themselves, after a brief training about software usage. A total of 10 clinicians from Imaging and Urology wards evaluated the already processed data and a total of 6 urologists directly tested the software producing printable model and provided their feedback.

2. Results

Software output was considered clinically accurate in most of tested data. 8/8 healthy kidneys were successfully segmented and each resulting part was exported to STL format. 2/2 kidneys were correctly segmented in terms of anatomical structures, while kidney stones were segmented with minimum data losses (smaller particles) due to denoising steps. In the hydronephrosis case, the routine was able to segment the healthy renal tissue left, precisely outlining the borders of the hydronephrosis; data did not allow to locate and segment vessels and ureter.

As for software usage, every user who tested the routine was able to successfully complete the assigned task. Feedback during task execution did not indicate notable difficulties in using the software. The average time required to complete the assigned task was 12 minutes. All result STL files were rated printable with no or limited post processing using FFF (Fused Filament Fabrication) technology. After gathering positive feedback about software output, a preliminary model was printed for clinical evaluation and was considered anatomically accurate in terms of macroscopic structures, relative positioning and dimension when compared to the original dataset, by 6/6 urologists.

3. Discussion

Software testing outlined positive preliminary results in term of accuracy and reception among its potential users. It can be further developed in terms of user interface and features. Among the most requested feature were an integrated routine to segment renal cysts and tumoral masses a tool to manually modify and add comments to segmentation results, and a more customizable result viewer.

As for output printable files, urologist already pointed at some useful applications such as uretero-nephroscopy simulation, diagnosis and communication support model, a renal tumor assessment model, a navigator model for laparoscopic surgery, a percutaneous nephrolithotomy simulator. These and other possible applications are closely linked to 3D printing technology development and to available printable materials; future developments should always relate to these crucial factors in order to have the best printing speed and quality.

4. Conclusions

The Kidney 3D Model Making Software produced clinically accurate results as well as files printable with limited post-processing. Although in an early version, the software had a good reception by clinicians and received positive feedback both from urologists and radiologists.

3D printable models fully met clinicians' expectation in terms of anatomical accuracy Further investigations will be conducted in order to actually 3D print models to develop an usable patient-specific simulator. These models could provide the important feature of patient-specific customization to the training routine, which is often not implemented in currently available simulators.

The whole study experience, developed in close cooperation with Rome Hospital "Policlinico Tor Vergata" Urology and Diagnostic Imaging Wards, met the medical professionals' wide interest and enthusiasm towards being actively involved in the development of innovative devices through 3D printing technologies. This interest and the recent massive development of 3D printing technologies make way to further possible applications.

References

[1] Y. Shiga et al, 1124 benefit of 3-dimensional printing in robotic laparoscopic renal surgery: Tangible surgical navigation using a patient-based 3-dimensional printed kidney. European Urology Supplements 1.13 (2014:e1124)

[2] J. C. Bernhard, S. Isotani, T. Matsugasumi et al. Personalized 3D printed model of kidney and tumor anatomy: a useful tool for patient education. World J Urology. 2015 July 11

[3] P. A. Yushkevich, J. Piven, H. Cody Hazlett, et al. User-guided 3D active contour segmentation of anatomical structures: Significantly improved efficiency and reliability. Neuroimage, 2006;31(3):1116-1128.

[4] A. Fedorov, R. Beichel, J. Kalpathy-Cramer, et al. 3d slicer as an image computing platform for the quantitative imaging network. Magnetic resonance imaging, 2012;30(9):1323-1341.

[5] W.D. Penny, et al., eds. Statistical parametric mapping: the analysis of functional brain images: the analysis of functional brain images. Academic press, 2011.

[6] R. Vivanti. Modeling and preoperative planning for kidney surgery. Master's thesis, The Selim and Rachel Benin School of Engineering and Computer Science, The Hebrew University of Jerusalem, Israel, June 2011.

[7] C. Rorden. "dcm2nii DICOM to NIfTI conversion." The source for neuroimaging: MRIcoron (2009).

[8] J. Shen. "Tools for NIfTI and ANALYZE image." (2011). Available online: https://www.mathworks.com/matlabcentral/leexchange/8797-tools-for-nifti-and-analyze-image

[9] C. Lewandowski. Export voxel data. Available online: https://www.mathworks.com/matlabcentral/fleexchange/43640-export-voxel-data

Visible photoluminescence of colour centres in LiF crystals exposed to 6 MV x ray clinical beams

R.M. Montereali[a,1], F. Bonfigli[a], M. Piccinini[a], M.A. Vincenti[a], R. Khan[b], J.E. Villarreal-Barajas[b]

[a]*ENEA C.R. Frascati, Department of Fusion and Technologies for Nuclear Safety and Security, Via E. Fermi 45, 00044 Frascati, Rome, Italy*
[b]*University of Calgary, Dep. of Oncology, 1331 29 St. NW, T2N 4N2, Calgary AB, Canada*

Abstract

Polished LiF crystals were irradiated by using 6 MV x rays produced by a clinical linear accelerator. The irradiation doses (absorbed dose to water) covered the 1-100 Gy range. Optical absorption spectra show stable formation of primary F defects up to a maximum concentration of 2×10^{16} cm^{-3}, while no significant M absorption band at around 450 nm, due to aggregate F_2 and F_3^+ colour centres, was detected. Under Argon laser excitation at 457.9 nm, photoluminescence spectra of the irradiated LiF crystals clearly exhibited the characteristic F_2 and F_3^+ visible broad emission bands. The integrated photoluminescence intensity of F_2 and F_3^+ defects was measured using a conventional fluorescence optical microscope under blue lamp illumination. In the investigated dose range, the integrated photoluminescence as a function of the irradiation dose shows a linear behavior. Even at the low volume densities of point defect obtained at the investigated doses, these preliminary experimental results are encouraging for further investigation of nominally pure LiF crystals as clinical dosemeters based on optical reading of photoluminescence emitted by radiation-induced visible-emitting colour centres.

Keywords: lithium fluoride; colour centres; photoluminescence; optical microscopy; dosimetry

5. Introduction

Among alkali halides, lithium fluoride (LiF) is a well-known material for photonic applications (Montereali, 2002) and dosimetry (McLaughin et al., 1980, Lakshmanan et al., 1996). It has also been deeply studied as far as basic optical properties of colour centres (CCs) are concerned (Fowler, 1968). LiF in pure and doped form has been successfully used as clinical dosemeter based on thermoluminescence for more than 60 years. In the last 20 years, optically stimulated luminescence (OSL) dosimetry has been commercially adopted mainly based on Al_2O_3:C (Yukihara et al., 2008). Among the advantages of OSL dosimetry there are fast evaluation, accuracy, wide dynamic range of measured dose, re-read capability and ability to perform imaging for dose mapping.

In order to determine the dose absorbed by human tissue under irradiation by ionising radiations, it is desirable to use tissue equivalent dosemeter materials, i.e. materials whose effective atomic number, Z_{eff}, is equal to 7.4 (McKeever et al., 1995). LiF is one of such materials because it is almost tissue equivalent, LiF Z_{eff} = 8.14, while Al_2O_3:C is characterized by Z_{eff} = 11.3 (McKeever et al., 1995). The "near" tissue equivalence of LiF and its optical and physical–chemical properties have encouraged research aimed to investigate the use of LiF as a dosemeter based on optical reading of photoluminescence (PL) emitted by radiation-induced CCs. CCs are produced in LiF crystals and films by irradiation with ionising radiations. The primary electronic defect is the F centre, which consists of an anionic vacancy occupied by an electron. Its absorption band, called F band, is located at about 248 nm. Up to now, PL originating from the F centres in LiF has not been detected unambiguosly (Baldacchini et al., 1993). The F_2 and F_3^+ aggregate centres (two electrons bound to two and three anion vacancies, respectively), stable and laser-active at room temperature (RT), possess almost overlapping broad absorption bands located at a wavelength about equal to 450 nm, which together form what is generally called M band (Nahum and Wiegand, 1967); under optical pumping in this spectral region they emit broad PL bands peaked at 678 nm and 541 nm for F_2 and F_3^+ centres, respectively (Nahum and Wiegand, 1967). Lately, PL of radiation-induced light-emitting CCs has also been explored in pure and doped LiF (Piaskowska et al., 2013). In the last decade, LiF crystals and thin films were also proposed for novel solid state luminescent imaging detectors with submicrometric spatial resolution for soft x rays up to energies of 80 keV (Montereali et al., 2013). Recently, their use was extended to advanced proton beam characterization and imaging (Piccinini et al., 2014, Piccinini et al., 2015).

In this work, the preliminary results of the optical investigation of radiation-induced CCs in 6 MV x rays irradiated pure LiF crystals in the clinically relevant dose range of 1-100 Gy are presented. Even at these low doses, optical

---

* Corresponding author. Tel.: +39 06 9400 5296; fax: +39 06 9400 5334.
E-mail address: rosa.montereali@enea.it.

absorption and laser-excited PL spectra were measured at RT and a conventional optical fluorescence microscope has been successfully used for the reading of the integrated visible PL signal (Villarreal-Barajas et al., 2015).

6. Materials and Methods

A set of nominally pure, commercially-available LiF crystals, dimensions $(5 \times 5 \times 0.5)$ mm^3, polished on both sides, were irradiated under full electronic equilibrium conditions using 6 MV x rays produced by a clinical linear accelerator (linac) at the Tom Baker Cancer Centre, Calgary. The irradiations were set to 1, 10, 20, 50 and 100 Gy. All the doses refer to doses to water. After irradiation, the LiF crystals were kept in the dark, but they were not protected from environment room light exposure during the optical absorption and PL measurements.

The optical absorption measurements of the irradiated and blank (unirradiated) LiF crystals were performed using a Perkin-Elmer Lambda 950 spectrophotometer at normal incidence. The spectral range was set to 190–800 nm with a 1 nm resolution.

The laser-induced PL measurements were performed at RT using a continuous wave mode Argon laser tuned at the wavelength of 457.9 nm, in order to simultaneously excite the visible PL of F_2 and F_3^+ CCs. The PL emission was spectrally analyzed in the 480-800 nm range by a monochromator (Horiba Jobin Yvon, Triax 320) equipped with a grating blazed at 500 nm, with a 2 nm resolution and detected by a photomultiplier (Hamamatsu H7422-50) using a lock-in technique. All the PL spectra were corrected for the instrumental spectral response.

The integrated PL signal emitted by the irradiated LiF crystals was also measured using a conventional wide-field optical microscope (Nikon Eclipse 80i) in fluorescence mode. The excitation light source was a mercury lamp OSRAM HBO 103W/2 (power 100 W). The used two-dimensional detector for the PL signal acquisition was a sCMOS camera (Andor Neo), 2560×2160 pixels, pixel size 6.5 micron, front illuminated and cooled at -30°C.

7. Results and discussion

Figure 1(a) shows the optical absorption spectra, in optical density (O.D.), of a blank LiF crystal and of the LiF crystals irradiated at 10, 50 and 100 Gy by 6 MV x rays. The F absorption band, peaked at around 248 nm, due to the stable formation of primary F CCs, is clearly observed for the LiF crystals irradiated at the highest doses (50 and 100 Gy). The M absorption band, due to F_2 and F_3^+ CCs, located at around 450 nm, is not clearly detected even for the highest irradiation doses used in this investigation. For the LiF crystals irradiated at 50 and 100 Gy, the concentration of F electronic defects was evaluated by the Smakula formula (Fowler, 1968) starting from the band peak absorption coefficient and the full width at half-maximum (FWHM) of each F absorption band, obtained by using a Gaussian best fit procedure. The estimated concentration of F defects was 1.25×10^{16} and 1.95×10^{16} cm^{-3} for the LiF crystals irradiated at 50 and 100 Gy, respectively.

Figure 1(b) reports the PL spectra of the LiF crystals irradiated at 10, 50 and 100 Gy, excited at the wavelength of 457.9 nm. Each Net PL spectrum shown in Fig. 1(b) is obtained by subtracting a blank PL spectrum (the PL spectrum of an unirradiated LiF crystal) from each measured PL emission of the irradiated samples. Each spectrum clearly presents the two characteristic broad emission bands, due to the aggregate F_2 and F_3^+ defects, centred around 678 and 541 nm, respectively. The separate contributions of the F_2 and F_3^+ emission to each PL spectrum were obtained by a best fit procedure with two Gaussian bands. The resulting spectral parameters of the F_2 and F_3^+ emission bands (peak position and FWHM) are in agreement with literature on LiF crystals (Baldacchini et al., 2000). The integrated PL signal associated with each PL spectrum, defined as the sum of the areas under the two Gaussian bands (sum of the contributions due to F_2 and F_3^+ CCs), as a function of the irradiation dose shows a linear behavior in the investigated dose range (Villarreal-Barajas et al., 2015).

F_2 and F_3^+ PL integrated intensity of the irradiated LiF crystals was also measured using a conventional fluorescence optical microscope under blue lamp illumination. In order to take into account potential variations of the lamp intensity and/or sCMOS sensitivity, an unirradiated LiF crystal was always positioned side by side close to the irradiated sample, as shown in Fig. 2(a) for the 50 Gy x rays irradiated LiF crystal. Optical images of the irradiated LiF crystals were sequentially acquired under this arrangement in identical experimental conditions. For each image, the integrated PL signals from two identical square areas of 0.975×0.975 mm^2, set at a distance of about 1.62 mm from the border line between the unirradiated and irradiated LiF crystal, see Fig. 2(a), were acquired. Their subtraction determines the "Net integrated PL" of each irradiated LiF crystal. Figure 2(b) reports the Net integrated PL as a function of the irradiation dose. Again, the Net integrated PL as a function of the irradiation dose shows a linear behavior in the investigated dose range, as evidenced by the linear best fit (see Fig. 2b). Figure 2b also reports the Net integrated PL as a function of the irradiation dose for LiF crystals irradiated with 5 MV x ray clinical linac at the lowest doses. Taking into account the energy spectrum characteristics of both x rays sources, the colour centres formation efficiency is expected to be very similar in both cases and the comparison of the experimental results seems to be significant. Again the Net integrated PL as a function of irradiation dose shows a linear behavior, which overlaps the previous one, in the clinically relevant

dose range (0.5-20 Gy). The linearity obtained for LiF crystals irradiated using 6 MV x rays, which is a very desirable feature of any radiation detector, is therefore confirmed.
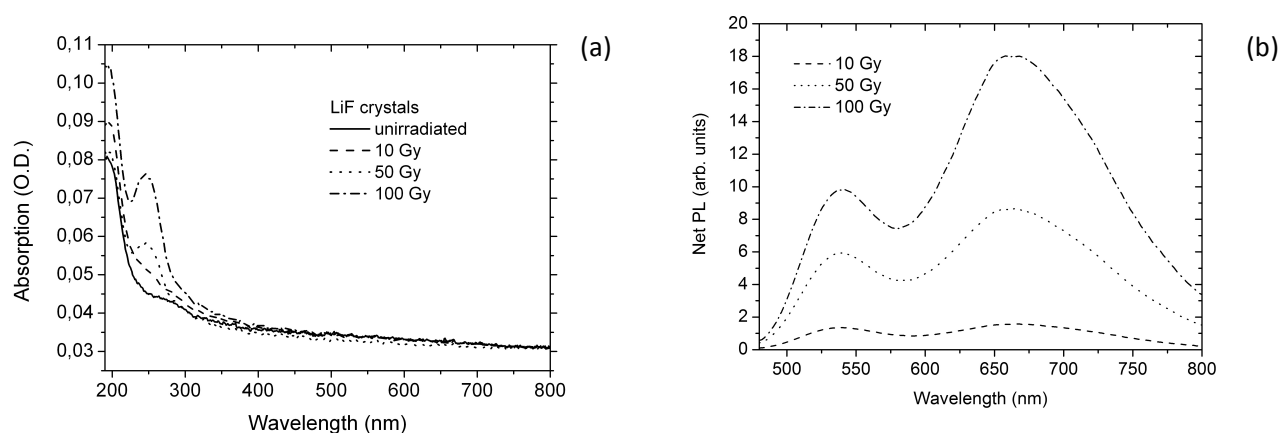

Fig. 1. (a) RT optical absorption spectra of 6 MV x rays irradiated LiF crystals at several doses. The spectrum of a blank crystal is reported for comparison (thickness 0.5 mm); (b) RT laser induced (457.9 nm) PL spectra of 6MV x ray irradiated LiF crystals at 10, 50 and 100 Gy under laser excitation at 457.9 nm
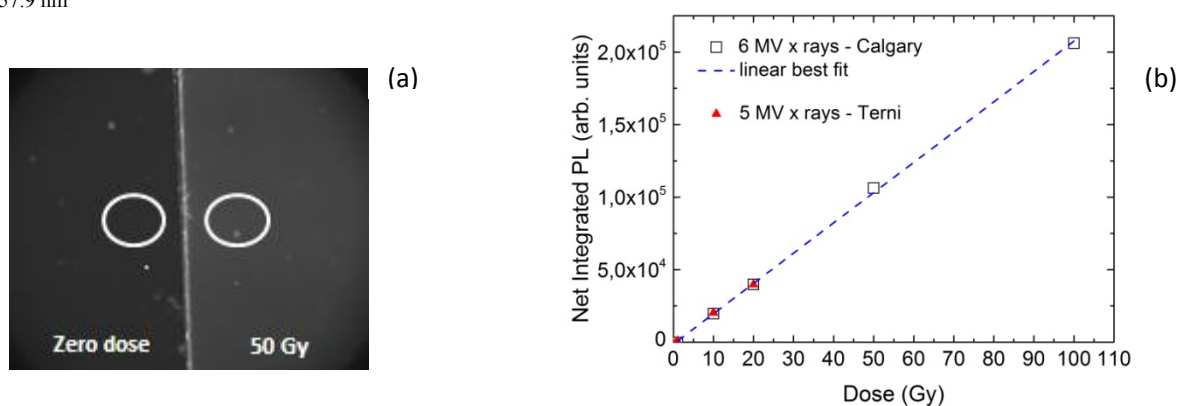

Fig. 2. (a) Fluorescence microscope image of a blank (zero dose), left, and the 50 Gy 6 MV x ray irradiated LiF crystal, right. The two white circles show the regions selected for the measurement of the integrated PL signal; (b) Fluorescence microscope Net integrated PL signal as a function of the absorbed dose for the irradiation by 6 MV x rays and linear best fit. Also the results obtained for irradiation by 5 MV x rays are reported

8. Conclusions

The use of pure LiF crystals as dosemeters based on optical reading of F_2 and F_3^+ PL, in the clinically relevant dose range (up to 100 Gy), has been investigated for 6 MV x rays. The linearity of the integrated PL response, due to F_2 and F_3^+ electronic defects, as a function of irradiation dose, measured by a fluorescence microscope system was demonstrated. This result is consistent with the optical response resulting from the laser induced PL spectra (Villarreal-Barajas et al., 2015). The linearity, which is a very desirable feature of any radiation detector, was obtained with a good reproducibility (within 5%). The reproducibility was derived from repeated PL measurements on the same irradiated LiF crystal at different doses. These PL evaluations were performed three times in a span of approximately 6 months. The PL evaluations for every LiF crystal was repeated at least three times giving a total of at least nine PL measurements per LiF crystal. A more comprehensive reproducibility investigation is required to assess the LiF crystal-batch reproducibility. This investigation will include the use of several crystals irradiated at the same dose.

Even at the low electronic defect densities (F concentrations below 2×10^{16} cm^{-3}) obtained at the investigated doses, these preliminary experimental results grant further investigation of CCs PL in LiF crystals for clinical dosimetry. Re-usability of the LiF crystals and laser induced PL reproducibility after thermal annealing requires additional investigation. In order to test the behavior of the optical PL response with x ray energy a more demanding investigation

would be required, in particular the relative response to x rays in the kilo Voltage range would be of significant relevance for clinical dosimetry applications.

Further experiments are under way to investigate the PL response in the 0-100 Gy dose range for irradiations with 70-270 MeV proton beams for hadron therapy by using the same batch of LiF crystals.

Further work is in progress to increase the PL reading sensitivity and to investigate the potential role of dopants.

Acknowledgements

References

Montereali, R.M., 2002. Point Defects in Thin Insulating Films of Lithium Fluoride for Optical Microsystems, in "*Handbook of Thin Film Materials*", 3: Ferroelectric and Dielectric Thin Films. Academic Press, p. 399.

McLaughlin, W.L., Miller, A., Ellis, S.C., Lucas, A.C., Kapsar, B.M., 1980. Radiation-induced color centers in LiF for dosimetry at high absorbed dose rates, NIM B 175, p. 17.

Lakshmanan, A.R., Madhusoodanan, U., Natarajan, A., Panigrahi, B.S., 1996. Photoluminescence of F-aggregate centers in thermal neutron irradiated LiF TLD-100 single crystals, phys. stat. sol. (a) 153, p. 265.

Fowler, W.B., 1968. *Physics of Color Centers*, W.B. Fowler, Editor. New York and London: Academic Press Inc.

Yukihara, E.G. and Mc Keever, S.W., 2008. Phys. Med. Biol. 53 R351.

McKeever, S.W.S., Moscovitch, M., Townsend, P.D., 1995. Thermoluminescence Dosimetry Materials: properties and uses, Nuclear Technology Publishing, Ashford, Kent TN23 1YW, England.

Baldacchini, G., Cremona, M., Grassano, U.M., Kalinov, V., and Montereali, R.M., 1993. Defects in Insulating Materials, O. Kanert and J.M. Spaeth, Editors. World Scientific, Singapore.

Nahum, J., and Wiegand, D.A., 1967. *Phys. Rev.* 154, p. 817.

Piaskowska, A., Marczewska, B., Bilsky, P., et al., 2013. Radiation Measurements 56, p. 209.

Montereali, R.M., Bonfigli, F., Nichelatti, E., Vincenti, M.A., 2013. Nuovo Cimento C 36, 2, p. 35.

Piccinini, M., Ambrosini, F., Ampollini, A., Carpanese, M., Picardi, L., Ronsivalle, C., Bonfigli, F., Libera, S., Vincenti, M.A., and Montereali, R.M., 2014. J. Lum. 156, p.170.

Piccinini, M., Ambrosini, F., Ampollini, A., Picardi, L., Ronsivalle, C., Bonfigli, F., Libera, S., Nichelatti, E., Vincenti, M.A., and Montereali, R.M., 2015. Photoluminescence of radiation-induced color centers in lithium fluoride thin films for advanced diagnostics of proton beams. Appl. Phys. Lett. 106, p. 261108.

Villarreal-Barajas, J.E., Piccinini, M., Vincenti, M.A., Bonfigli, F., Khan, R., Buono, E., Italiani, M., Pimpinella, M., Montereali, R.M., 2015. Visible photoluminescence of colour centres in LiF crystals for absorbed dose evaluation in clinical dosimetry, IOP Conf. Series: Materials Science and Engineering 80, 12020, doi:10.1088/1757.

Baldacchini, G., De Nicola, E., Montereali, R.M., Scacco, A., and Kalinov, V., 2000. J. Phys. Chem. Solids 61, p. 21.

Three-dimensional structure of human 5-LOX in solution: new insights from SAXS analysis

A. Sabatucci[a], C.B. Angelucci[b], D. Steinhilber[c], M. Simonetti[a], M. Maccarrone[de+], E. Dainese[ae+2]

[a] *Faculty of Biosciences, University of Teramo, Teramo, 64100, Italy*
[b] *Faculty of Veterinary Medicine, University of Teramo, Teramo, 64100, Italy*
[c] *Institute of Pharmaceutical Chemistry, Goethe University Frankfurt, Germany*
[d] *Center of Integrated Research, Campus Bio-Medico University of Rome, Italy*
[e] *European Center for Brain Research (CERC)/Santa Lucia Foundation, Rome, Italy*
[+] *Equally senior authors.*

Abstract

Human 5-Lipoxygenase (5-LOX) is implied in the biosynthesis of leukotrienes, lipid mediators of inflammation. We performed a combined SAXS and SE-HPLC study to determine the oligomerization state of wild-type human 5-LOX in solution. We also verified if the native protein shows structural differences in comparison to the published crystal structure of a mutant human 5-LOX where substitutions have been introduced to stabilize the enzyme. Our results show that 5-LOX consists mainly of two dimeric species with the same symmetry of the crystal structure, but distinct hydrodynamic volumes because of a different hydration status/ degree of flexibility. Monomeric species - compatible with the crystal structure - are also present in solution at low percentage. The question is open on possible effectors that might modulate monomer/monomer interactions and monomer/dimer equilibrium.

Keywords: SAXS; SE-HPLC; 5-LOX; oligomerization

---

1.   Introduction

Lipoxygenases (LOXs) form a heterogeneous family of fatty acid dioxygenases that are widely distributed in plants and animals (Dainese et al., 2010; Radmark et al., 2015).

Human 5-LOX is implied in the biosynthesis from arachidonic acid (AA) of leukotrienes, lipid mediators of inflammation (Radmark, et al., 2015). 5-LOX activity is short-lived, apparently in part because of an intrinsic instability of the enzyme. The crystal structure of a stable mutant human 5-LOX, lacking putative membrane insertion amino acids, has been solved at 2.4 Å resolution (Gilbert et al., 2011).

The unique feature of the last generation synchrotron radiation beamlines, which allow to perform a combined approach of size-exclusion liquid chromatography (SE-HPLC) followed by SAXS, is to obtain structural information on complex protein systems like 5-LOX in solution.

Both SE-HPLC and SAXS give information on the volume and molecular mass of proteins but these structural parameters can be derived starting from different physical principles.

It is well known that in SE-HPLC the elution profile of proteins is related to their hydrodynamic radius (R_H), defined by the frictional coefficient (f) in a viscous medium as follows:

$$f = 6\pi R_H \tag{1}$$

By definition, R_H is the radius of a hypothetical hard sphere that diffuses with the same speed as the particle under examination. In practice, macromolecules in solution are non-spherical, dynamic (tumbling), hydrated and solvated. As such, the radius calculated from the diffusional properties of a particle is indicative of its apparent size. Taking into account that the particle is dynamic, hydrated/solvated, this radius can therefore be bigger than the actual size of the macromolecule. Consequently, the molecular mass calculated from this parameter with a hard sphere approximation can easily be over-estimated.

Instead, from the analysis of the SAXS profile, the molecular mass (M) of a protein in solution can be derived from the scattered intensity at zero angle (I(0)) extrapolated from the analysis of the Guinier region (Guinier and Fournet, 1955). In fact, in the low- angle region, the Guinier law can be applied to fit the scattering intensity I(q):

$$I(q) = I(0)\,\exp\!\left(-\frac{q^2 R_g^2}{3}\right) \tag{2}$$

Where q is the scattering vector, $q=(4\pi/\lambda)\sin\theta$, 2θ being the scattering angle; and R_g is the radius of gyration

---

of the equivalent sphere.

And, if the measurement is performed in an absolute scale (see e.g. (Koch, et al., 2003)), the I(0) is proportional to the molecular mass and volume as follows:

$$ = (0)\frac{^2}{(1- _0)^2} \qquad\qquad (3)$$

Where μ is the ratio between the molecular mass of the protein and the number of electrons in the particle (a constant value close to 1.87); ρ_0 is the average electron density of the solvent (electrons nm^{-3}), Ψ is ratio of the volume of the particle to its number of electrons and N_A is Avogadro's number.

It must be noted that the experimental scattering curve results from the excess scattering density of the macromolecules in solution with respect to the solvent. For this reason, from the analysis of the scattering pattern, it is more probable to under-estimate the value of the volume and, thus, of the molecular mass and of the radius of gyration, especially for non spherical, highly flexible molecules.

Thus, the integration of the structural information obtained from the coupling of these two techniques on proteins in solution, as in the last generation HPLC/SAXS synchrotron beamlines, is crucial for non-globular flexible molecules, giving information on their degree of aggregation, mobility and hydration, as well as on their spatial arrangement in solution. This approach allowed us to determine the oligomerization state of the native human 5-LOX in solution, revealing the presence of two distinct dimeric species differing in hydrodynamic volume and a low percentage of monomers, well fitting the crystal structure symmetry.

2.   Materials and Methods

Pure human 5-LOX was purified as already described (Steinhilber et al., 2012) and exhaustively dialyzed against Na Phosphate buffer 50 mM pH 7.0.

SAXS measurements were carried out at the SWING SAXS/WAXS beamline (synchrotron Soleil, Paris, France) in SE-HPLC setup. In this setup, the sample is injected into the HPLC system and the eluate flows from the column output to a glass capillary sample holder hit by the X-ray beam. The beam was monochromatic at a wavelength of 1.033 Å. The 2D detector was positioned at a sample-to-detector distance of D= 2940 m, determining a scattering vector q- range of 0.003<q<0.4 Å^{-1}.

A human 5-LOX solution volume of 50 µl was injected in the SE-HPLC system at a buffer flux of 250 µl/min to a BioSep-SEC-S3000 (Phenomenex®) gel filtration column with an exclusion range 5-700 kDa. Column calibration was performed with 3 protein standards, namely human Retinol Binding Protein (23 kDa), soybean Lipoxygenase-1 (94 kDa), human thyroglobulin (670 kDa).

While recording the absorbance of the sample in the HPLC system at a wavelength of 280 nm, 180 frames of the scattering intensity in the 2D detector were recorded (2000 ms life time, 1000 ms dead time) 30 min. after sample injection.Within this series, the frames corresponding to the chromatographic peaks - characterized by constant intensity and radius of gyration - were averaged. Finally, the signal of the buffer was subtracted to the averaged frames.

Data reduction was performed with the program Foxtrot (developed by the SWING team). Further analysis was performed using the program suite ATSAS (Petoukhov et al., 2012). In detail, PRIMUS allowed us to calculate the radius of gyration of the protein species in solution. The distance distribution function p(r), giving the electronic distribution around the center of gravity and the maximum diameter D_{max} of the particle, was determined using the indirect Fourier transform method as implemented in the program package GNOM. The theoretical curve from the crystal structure of 'stable LOX', pdb entry 3O8Y.pdb (Gilbert et al., 2011), was obtained with the program crysol (version 2.7). The best fit of this curve vs. the experimental scattering patterns was performed with the same program. The *ab initio* low-resolution envelopes were calculated from the p(r) functions as dummy atom models (DAM) using the program suite DAMAVER. For each model, ten independent calculations were performed, averaged and filtered. The superposition of the low-resolution DAM models to the crystal structures was performed with the program supcomb 2.0.

3D model visualization was performed with the program 'Accelrys 2D visualiser'.

3.   Results

Wild type human 5-LOX eluted from the SE column in three distinct peaks at retention times respectively of 31.211 min. (peak 1), 32.702 min. (peak 2) 35.654 min. (peak 3). The relative weights of the peaks with respect to the total fraction are reported in table 1.

From column calibration, we estimated for each species the following molecular weights: peak 1, 301±19 kDa; peak 2, 187±19 kDa; peak 3, 73±19 kDa. From this result, three different oligomeric species were supposed to be present in solution.

We then analyzed the scattering patterns of the three peaks (fig.1) and the relative p(r) functions were calculated.

From these last, a maximum diameter D_{max} respectively of 140 Å (peak 1), 132 Å (peak 2) and 92 Å (peak 3) was derived.

DAM models of the three SE elution peaks (fig.2) revealed that peak 1 and 2 are both compatible with the symmetry of 5-LOX dimers, where peak 1 is characterized by a slightly higher displaced solvent volume with respect to peak 2 (see table 1). This result clearly shows that the two SE elution peaks do not correspond to different oligomeric states of the human 5-LOX; rather, to two structurally distinct dimeric species, the first one characterized by higher hydrodynamic and gyration radius, (see table 1) clearly indicating a more hydrated/flexible/protein in solution with respect to peak 2. Finally, peak 3 well fits the crystal structure of the 5-LOX monomer (see chi-values in table 1),4re indicating that the stable mutant enzyme has the same structure of the wild type protein in solution.

We showed that plant and mammalian lipoxygenases have different degrees of conformational flexibility and thermal stability (Mei, et al., 2008). It has been recently suggested that, unlike soybean LOX-1, that we previously showed by SAXS to be organized as a stable monomer (Dainese et al., 2005), 5-LOX could form a dimeric complex, where one monomer catalyzes the generation of 5-HPETE, which is then transferred to the other monomer for the formation of leukotrienes (Hafner et al., 2011). Our results confirm these observations and open an interesting question on the functional meaning of the presence of two different dimeric species and on the possible effectors that might modulate monomer/monomer interactions, and hence monomer/dimer equilibrium, leading to a specific functional regulation of 5-LOX *in vivo*.
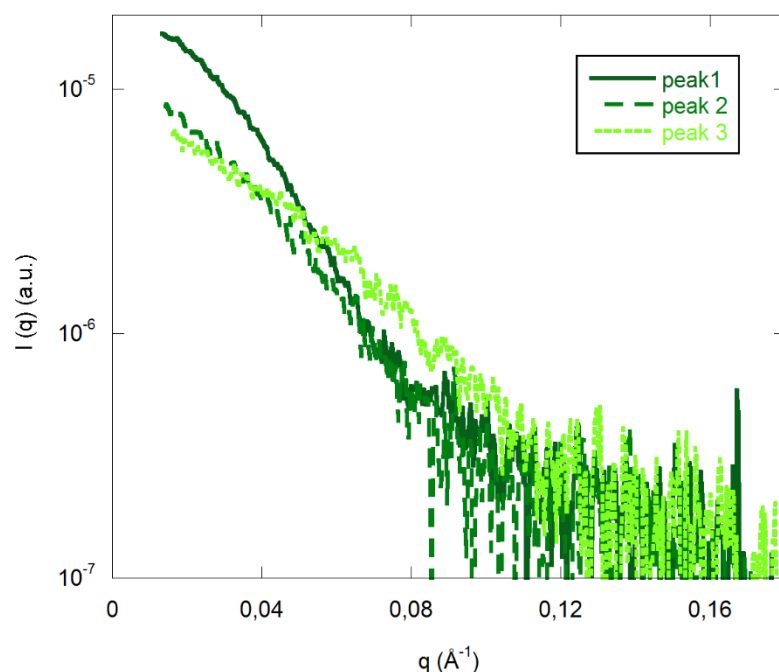

Fig. 1: Scattering patterns of the three SE-HPLC peaks characterizing human 5-LOX. Dark green straight line: Peak 1; green dashed line: Peak 2; light green dotted line: Peak 3.
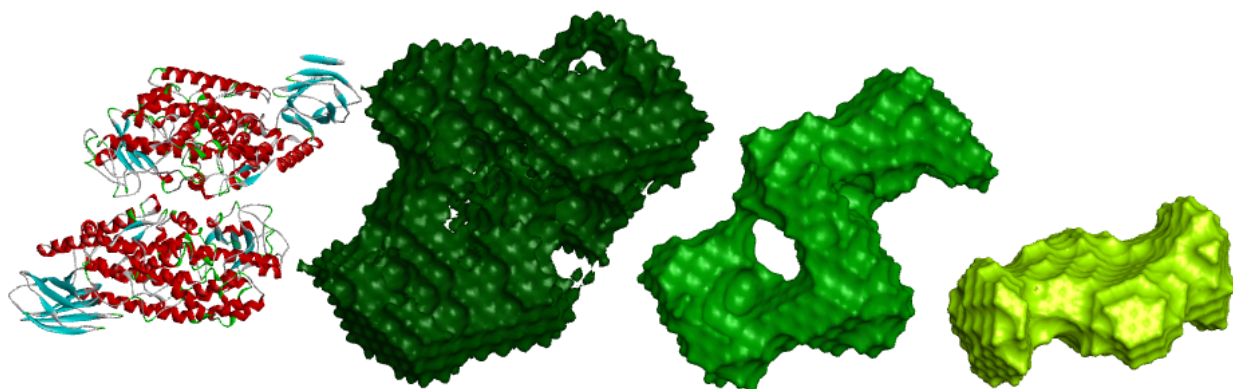
Fig.2 From left to right: crystal structure of stable human 5-LOX (Gilbert et al., 2011); low-resolution DAM models of the three 5-LOX species detected in solution as different SE-HPLC peaks. The models clearly indicate that both peak 1 (dark green) and peak 2 (green) are dimers while peak 3 is a monomer.

Table 1. Overall structural SAXS parameters of each SE-HPLC peak of human 5-LOX

	Rg (Å)	Dmax (Å)	Se-HPLC peak Rel. weight (%)	Fitting parameters vs stable 5-LOX crystal*			
				DIMER			
				Theor. Rg (Å)	Exp Rg (Å)	V (Å^3)	Chi value
Peak1	47.4±0.9	140±1	45.5	39.55±0.1	46.66±0.12	208614	3.763
Peak 2	39.9±0.4	132±1	24.3	39.05±0.1	43.33±0.33	199882	1.109
				MONOMER			
Peak3	30.8±0.2	92±1	30.2	29.10	31.88±0.29	89414	1.135

*Parameters calculated with the program crysol. The volume refers to the total displaced solvent volume.

Acknowledgements

References

Dainese, E., Angelucci, C. B., Sabatucci, A., De Filippis, V., Mei, G., Maccarrone, M., 2010. A novel role for iron in modulating the activity and membrane-binding ability of a trimmed soybean lipoxygenase-1, FASEB J. 24, p. 1725.

Radmark, O., Werz , O., Steinhilber, D., Samuelsson, B., 2015. 5-Lipoxygenase, a key enzyme for leukotriene biosynthesis in health and disease, Biochim Biophys Acta 1851, p. 331.

Gilbert, N. C., Bartlett, S. C., Waight , M. T., Neau, D. B., Boeglin, W. E., Brash, A. R., Newcomer, M. E., 2011. The structure of human 5-lipoxygenase, Science 331, p. 217.

Guinier, A., Fournet , G., 1955. Small-Angle of X-rays. Wiley, New York.

Koch, M., Vachette, P., Svergun, D. I., 2003. Small-Angle Scattering: a view on the properties, structures and structural changes of biological macromolecules in solution, Quarterly Reviews of Biophysics 36, p. 147.

Steinhilber, D., Hofmann, B., Rödl, C. B., Kahnt, A. S., Maier, T. J., Michel, A. A., Hofmann, M., Rau, O., Awwad, K., Pellowska, M., Wurglics, M., Wacker, M., Zivkovic, A., Fleming, I., Schubert-Zsilavecz, M., stark, H., Schneider, G., 2012. Molecular pharmacological profile of a novel thiazolinone-based direct and selective 5-lipoxygenase inhibitor, Br J Pharmacol 165, p. 2304.

Petoukhov, M. V., Franke, D., Shkumatov, A. V., Tria, G., Kikhney, A. G., Gajda, M., Gorba, C., Mertens ,H. D., Konarev, P. V., Svergun, D. I., 2012. New developments in the ATSAS program package for small-angle scattering data analysis, J. Appl. Cryst. 45, p. 342.

Mei, G., Di Venere, A., Nicolai, E., Angelucci, C. B., Ivanov, I., Sabatucci, A., Maccarrone, M., 2008. Structural properties of plant and mammalian lipoxygenases. Temperature-dependent conformational alterations and membrane binding ability, Biochemistry 47, p. 9234.

Dainese, E., Sabatucci, A., van Zadelhoff, G., Angelucci, C. B., Vachette, P., Veldink, G. A., Maccarrone, M., 2005. Structural stability of soybean lipoxygenase-1 in solution as probed by small angle X-ray scattering, J Mol Biol 349, p. 143.

Hafner, A. K., Cernescu, M., Hofmann, B., Ermisch, M., Hornig, M., Metzner, J., Steinhilber, D., 2011. Dimerization of human 5-lipoxygenase, Biol Chem 392, p. 1097.

The low-energy Proton Beam for Radiobiology Experiments

at the TOP-IMPLART facility

M. Vadrucci*, A. Ampollini, G. Bazzano, L. Picardi, C. Ronsivalle,

ENEA Radiation Sources Laboratory, Frascati Research Center via E. Fermi 45, 00044Frascati (RM), Italy

Abstract

The TOP (Oncological Therapy with Protons)-IMPLART (Intensity Modulated Proton Linear Accelerator for RadioTherapy) accelerator is a facility for proton-therapy under construction in ENEA C. R. Frascati Radiation Sources Laboratory in collaboration with ISS and IFO. It is a completely linear pulsed accelerator consisting of a 7 MeV injector followed by a high frequency booster up to 150 MeV. A vertical beam extraction-line at the exit of injector has been devoted to in-vitro radiobiology experiments for the characterization of the low-energy proton beam.

Irradiation experiments were carried out on V79 and CHO Chinese hamster cells. Both cell lines have been widely used in radiobiology studies with different radiation qualities thus allowing the evaluation and the comparison of results.

In order to carry out the biological characterization of the facility, the radiation responses of V79 and CHO cells have been evaluated in terms of clonogenic survival. Moreover, a protocol of Micronuclei Assay for the in situ evaluation of radiation induced DNA damage has been adapted to the specific exposure conditions of the vertical proton beam.

Preparatory irradiations have been performed with 5 MeV (incident LET= 7.7 keV/μm in MS20) protons extracted in air and impinging on cells; the clonogenic survival is eveluated in the dose range 0.2-8 Gy.

The preliminary dose-response data have a linear-quadratic arrangement. Future developments to improve precision and reproducibility of measurements are also described.

Keywords: proton beams, *in-vitro* radio-biology experiments.

1. Introduction

Proton beam therapy has become a clinical standard treatment in radiotherapy for cancer care of specific types of tumor which are problematic to treat by conventional radiotherapy with photons (C.E. Hill-Kayser et al., 2011); (M. Durante et al., 2013); (A. Zurlo et al., 2000); (M. Vadrucci et al., 2015).

Protons allow interactions with high spatial selectivity compared to X-rays because of the energy deposition of the particle beam in the tumor target agrees a uniform coverage with millimetric precision. This characteristic, due to the presence of the Bragg peak at the end of the path and the lower lateral diffusion, make protons particularly suitable for tumors located close to critical structures (D.R. Olsen et al., 2007).

There are several dedicated protontherapy facilities in the world and recently have been launched also in Italy two new centers in addition to the existing CATANA, the first Italian protontherapy center for the ocular melanoma treatment: CNAO where protons as well as carbon ions (and oxygen in the near future) may be used (CNAO, 2012); (M. Krengli, 2004) and APSS-Trento where only proton beams are available (APSS, 2014).

---

* Corresponding author. Tel.: +39 06 9400 5154 Fax: +39 06 9400 5334.
E-mail address: monia.vadrucci@enea.it.

At the ENEA-Frascati research center the first protontherapy facility employing a full linear accelerator scheme, based on high frequency technology for intensity modulated cancer treatments, is under construction in the framework of the Italian TOP-IMPLART (Oncological Therapy with Protons-Intensity Modulated Proton Therapy Linear Accelerator for Radio-Therapy) Project (C. Ronsivalle et al., 2011).

The partners involved with ENEA in the program, funded by the local government (Regione Lazio), are the Italian National Institute of Health (ISS) and the Italian Cancer Institute Regina Elena (IFO), the largest oncological hospital in Rome, where protontherapy center will be installed.

The TOP-IMPLART facility will have a dedicated beam line output to radio-biology experiments, aimed to acquire data to implement in clinical protocol, and moreover will provide proton beams for tumor treatment. Therapeutic beams have an energy range between 70 and 230) MeV, corresponding to a path in tissue from 4 cm (for the ocular tumors treatment) to 36 cm (for the deep tumors treatment); dividing the target in many elementary volumes, called voxels, where the prescribed dose is sent using a pencil beam.

As for the radio-biology the TOP-IMPLART project includes in vivo and in vitro experiments and the work program covers irradiation activities for studies of cells and small-animal behavior with (0.5 to 7) MeV and >18 MeV proton energies respectively. For this purpose, during the first two years funded, we designed and carried out preparatory in-vitro experiments pointed to the realization of the correct irradiation and control set-up, as described below: next paragraphs illustrate the planned in-vitro radiobiology experimental campaign, the TOP-IMPLART facility, the first tests on cells and a presentation of the expected developments.

2. Materials and methods

The TOP-IMPLART accelerator is currently composed by a 7 MeV injector, and two 3 GHz LINAC structures reaching the energy of 18 MeV (P. Nenzi et al., 2015); (C. Ronsivalle et al., 2015) and a third accelerating (up to 27 MeV) module under commissioning.

2.1. In-vitro radio-biology experimental campaign

For the optimal operational condition of the proton irradiation facility physical investigations are necessary: energy loss assessment, scattering phenomena evaluation and dose distribution control. These analyses have to be complemented then by biology-oriented studies, considering the mechanisms of biological effects by means of available literature data and adequate models.

In order to carry out the biological characterization of the TOP-IMPLART facility we want to evaluate the radiation responses of two cell lines (V79 and CHO) in terms of clonogenic survival and to adapt the specific exposure conditions of the vertical proton beam to the protocol of micronuclei assay for the in-situ analysis of radiation induced DNA damage. On the basis of the availability of biological data, the linear quadratic model is the right one to calculate the biological effectiveness in the low-dose proton plan. The cell surviving fraction, SF, as a function of the total dose, D, is then expressed by the equation 1:

$$SF = \exp\left(-\alpha \cdot D - \beta \cdot D^2\right) \qquad (1)$$

where the α and β parameters are energy-dependent and are calculated for each separate dose contribution at different cells depths (N Tilly et al., 2005). When the total distance travelled by the proton is kept short enough so that the total energy lost is only a small fraction of the initial energy one has the so-called track-segment conditions: the length of the track is such that longitudinal equilibrium of the fluence of secondary electrons in the volume of interest is established and a proper determination of the dose is obtained by the equation 2:

$$D(Gy) = 1.6 \ 10^{-9} \ F \ (\text{particles cm}^{-2}) \ LET \ (\text{keV } m^{-1}) \ ^{-1} \ (g \, cm^{-3}) \qquad (2)$$

where F is the proton beam fluence, LET is evaluated at the cell mid-plane monolayer by the SRIM code (J.F. Ziegler, 2010), ρ is the density of the medium.

To achieve this configuration we choose to perform the irradiations with 6 μm monolayers of cells (M. Belli et al., 1998). A practical arrangement to perform experiments with cells growing in monolayer is to make them adherent on a mylar sheet. Using a suspension protons have to impinge from the bottom of the cells sample holder. This is the reason why the set-up of the vacuum line of the TOP-IMPLART accelerator was modified with an extraction segment in which the beam runs vertically upwards. The cells sample holder is a cylindrical stainless steel Petri dish, 1.3 cm inner diameter having at

the base a 60 μm mylar sheet on which the cells adhere (M. Vadrucci et al., 2014) as designed in the LNL Laboratory where the experiments we take as a reference were done by Belli et al. (M. Belli et al., 1998)

The investigated dose-range has been chosen as 0.2 to 8 Gy in order to compare the results with the said literature.

2.2. The radio-biology Irradiation Facility and Dosimetry

The facility for radiobiological irradiation is the first segment of the TOP-IMPLART accelerator (the low energy section). It is composed by a proton injector (consisting of a 30 keV DuoPlasmatron Source, a Radio Frequency Quadrupole and a Drift Tube Linac, both operating at the frequency of 425 MHz) able to give a continuously variable energy beam from 3 to 7 MeV, followed by a transport line with magnetic quadrupoles to match the proton beam in the transverse planes with the medium energy accelerating structures (L. Picardi et al., 2014); (C. Ronsivalle et al., 2015). A magnetic dipole placed after the first couple of quadrupoles bends particles in the vertical beam line dedicated to the in-vitro radiobiology experiments described in this paper.

The vertical line includes a 2 mm diameter aluminum collimator and a 2 μm gold foil scatterer in order to have an homogeneous irradiation of the biological sample.

The beam extraction in air is realized through a circular Kapton window 50 μm thick positioned at 50 cm from the scatterer. The flange of the beam exit window was designed to clamp a special sample holder (fig.1).
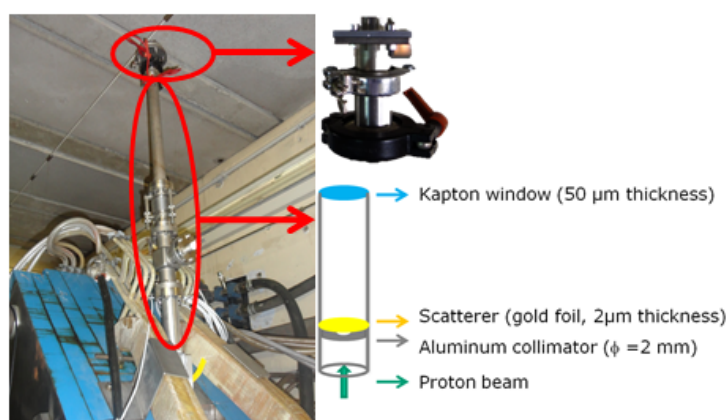

Fig. 1. (a) picture of the radio-biology vertical line; (b) sketch of the vertical line and its terminal with the cells sample holder

The energy of the protons produced by the injector, measured by the bending magnet used as a spectrometer, is 6.2 MeV and is degraded down to 5 MeV on the biological sample after the mylar sheet according to SRIM code calculations.

To calculate and measure in real-time the absorbed dose in the in-vitro experiments an in air Faraday cup was realized. The detector has twofold purpose. The first one is to hold up the sample always in the same position and orientation with respect to the impinging proton direction: the Petri dish (containing cells) is inserted in a metallic cylindrical armor wedged in the final flange of the vertical beam line. The second one is to monitor the beam undergoing the biological medium: the detector shield isolates the inner environment from electrostatic field and collects the trespassing electric charges.

The apparatus is connected to an amplifier (LM108, AV = 80) and a two channels digitizer with external trigger (NI-USB-5102) remotely controlled: signals are acquired for 500 μs, with a vertical resolution of 8 bits (about 8 mV), in correspondence of the accelerator trigger and a specifically designed LabView platform allows to change the acquisition settings, to display and to process on-line the data. The program records the number of spill acquired (giving a measure of the duration of irradiation), the mean intensity of the individual spill and the its standard deviation (creditable with the accelerator stability while a single acquisition). This integral intensity of the measured current, the Monitor Unit (MU), is associated with a value of absorbed dose measured by Gafchromic EBT3 films (ISP) calibrated at the LNL test-facility (M. Belli et al., 1987); (M. Vadrucci et al., 2015) using the same experimental setup (during the EBT3 calibration experimental campaign the films were placed over a 60 μm thick mylar sheet within the stainless steel Petri dish instead of the cells and their culture medium). With this arrangement 99.4% of the 5 MeV proton beam is transmitted over the film EBT3 (calculated by SRIM code) hence the MU reading, in volts, is connected to the absorbed dose through the film, in Gy.

3. Firsts test on cells and perspectives

The planned experimental campaign includes two phases: after a first phase consisting in a characterization of the 5 MeV proton beam aimed to a comparison with literature data (M. Belli et al, 1998) the interest from the standpoint of radiobiology is to investigate the behavior in terms of cell survival and micronuclei of cells irradiated at lower energies in a range not yet explored. Preparatory irradiation tests were carried out in the selected dose-range 0.2 to 8 Gy with V79 and CHO cells to verify that the TOP-IMPLART operative conditions described above are suitable for the radio-biology studies observing that the vertical line realized and dedicated to radiobiology is functional to the scientific targets. The preliminary collected data show the expected shape of the surviving cells fraction curve versus dose (M. Belli et al, 1998) characterized by an initial shoulder followed by a straight placement.

However some problems of data reproducibility prevented to retrieve confident values of α and β parameters in the equation (1): the low doses regime (≤ 0.5 Gy) is affected by a larger error due to the transient in the pulsed operation and also the precision of the response of the on-line dose control system has to be improved. In order to overcome these limits 1) we are providing a rotating multi-sample holder remotely piloted that will allow to operate irradiations of samples in series with the beam of particles continuously active and 2) we are also developing a fluence measuring system based on a silicon sensor placed off axis with respect to the beam measuring the fraction of scattered protons by the gold foil (used to uniformly spread the proton beam): this fraction is proportional to the number of protons reaching the biological sample. Moreover in parallel a protocol (dilution, incubation and fixing) of Micronuclei Assay has been adapted to analyze the DNA damage in the specific exposure conditions (M. A. Tabocchini, 2015) programmed for the final tests that will include microscope analysis.

References

A. Zurlo, A. L. (2000). The role of proton therapy in the treatment of large irradiation volumes: A comparative planning study of pancreatic and biliary tumors. *Int. J. Radiat. Oncol. Biol. Phys., 48*, 277-288.

APSS. (2014). *http://www.iba-protontherapy.com/sites/default/files/pt/media%20center/PT_Today_September_2014.pdf*.

Belli et al, R.-L. r.-9. (1998).

C. Ronsivalle et al. (2011). The TOP IMPLART Project. *Eur. Phys. J Plus, 126*(7), 68.

C. Ronsivalle, L. P. (2015). First acceleration of a proton beam in a Side Coupled Drift tube Linac. *Europhysics Letters (2015), 111, 14002*.

C. Ronsivalle, L. P.-5. (2015).

CNAO. (2012). *http://www.cnao.it/documents/2012/first_patient_with_carbon_ions-13-11-12.pdf*.

D.R. Olsen, O. B. (2007). Proton therapy - a systematic review of clinical effectiveness. *Radiother Oncol. , 83*(2), 123-32.

Durante, J. L. (2013). Charged particle therapy—optimization, challenges and future directions 10. *Nature Reviews Clinical Oncology, 10*, 411-424.

Frykholm, I. N. (2007). D.R. Olsen, O.S. Bruland, G. Proton therapy - a systematic review of clinical effectiveness. *Radiother Oncol., 82*(2), 123-32.

Hill-Kayser C.E., B. S. (2011). *1*(24), 1-9.

ISP. (n.d.). *ISP, Wayne-NJ, http://www.ashland.com/Ashland/Static/Documents/ASI/Advanced%20Materials/gafchromic-ebt3.pdf*.

J.F. Ziegler, J. B.-T.-1.-2. (2010).

L. Picardi, A. A.-4. (2014).

M. A. Tabocchini, A. A. (2015). Top-implart Linear Accelerator for Proton Therapy: Layout and First Radiobiological Results at Low Energy. *4-PS8F-10.* Kyoto: ICRR2015.

M. Belli, R. C.-5. (1987).

M. Krengli, R. O. (2004). Medical aspects of the National Centre for Oncological Hadrontherapy (CNAO - Centro Nazionale Adroterapia Oncologica) in Italy. *Radiother. Oncol., 73*(2), S21-S23.

M. Vadrucci et al., E. a.-F.-7. (2014). Experimental activity in the ENEA-Frascati irradiation facility with 3-7 MeV protons. *Proceedings of IPAC2014* (pp. 2156-58). Dresden, Germany: IPAC2014.

M. Vadrucci, G. E. (2015). Calibration of Gafchromic EBT3 for absorbed dose measurements in low energy proton beam and 60Co. *Med Phys., 42*(8), 4678.

M. Vadrucci, P. F. (2015). Cost-effective analysis for protontherapy versus advanced radiotherapy treatment in prostate cancer. *Int. J. of Particle Therapy - proceedings to the 54th PTCOG, 18-23 May 2015 san Diego, California*.

N Tilly, J. J.–2. (2005).

P. Nenzi, A. A.-I.-4. (2015).